2022-01

Seasonal and long-term variations in leaf area of Congolese rainforest

This work was made openly accessible by BU Faculty. Please share how this access benefits you. Your story matters.

Version	Accepted manuscript
Citation (published version):	Y. Sun, Y. Knyazikhin, X. She, X. Ni, C. Chen, H. Ren, R.B. Myneni. 2022. "Seasonal and long-term variations in leaf area of Congolese rainforest." Remote Sensing of Environment, Volume 268, pp. 112762 - 112762. https://doi.org/10.1016/j.rse.2021.112762

https://hdl.handle.net/2144/44857
Boston University

1 **Seasonal and long-term variations in leaf area of Congolese rainforest**
2

3 Yuanheng Sun[1,2], Yuri Knyazikhin[1], Xiaojun She[1,3], Xiangnan Ni[1,4], Chi Chen[1,5], Huazhong Ren[2]
4 and Ranga B. Myneni[1]
5

6 [1]Department of Earth and Environment, Boston University, Boston, MA 02215, USA
7 [2]School of Earth and Space Sciences, Peking University, Beijing, China
8 [3]School of Geographic Sciences, Southwest University, Chongqing, China
9 [4]Department of Earth and Environmental Sciences, Xi'an Jiaotong University, Xi'an, China
10 [5]Department of Earth and Environmental Sciences, Lawrence Berkeley National Laboratory,
11 Berkeley, CA 94720, USA
12

13

14 **Highlights**
15 • Seasonal variations of leaf area in Congolese rainforests co-vary with the unique bimodal
16   precipitation pattern.
17 • MISR and EPIC angular reflectance signatures corroborate the seasonal behavior of leaf area.
18 • No widespread decline in leaf area is confirmed with MISR and EPIC BRF angular signatures.
19 • Localized long-term precipitation decline has minimal impacts on leaf area over the past two
20   decades.

21 **Abstract**

22 It is important to understand temporal and spatial variations in the structure and photosynthetic

23 capacity of tropical rainforests in a world of changing climate, increased disturbances and human

24 appropriation. The equatorial rainforests of Central Africa are the second largest and least

25 disturbed of the biodiversly-rich and highly productive rainforests on Earth. Currently, there is a

26 dearth of knowledge about the phenological behavior and long-term changes that these forests are

27 experiencing. Thus, this study reports on leaf area seasonality and its time trend over the past two

28 decades as assessed from multiple remotely sensed datasets. Seasonal variations of leaf area in

29 Congolese forests derived from MODIS data co-vary with the bimodal precipitation pattern in this

30 region, with higher values during the wet season. Independent observational evidence derived from

31 MISR and EPIC sensors in the form of angular reflectance signatures further corroborate this

32 seasonal behavior of leaf area. The bimodal patterns vary latitudinally within this large region.

33 Two sub-seasonal cycles, each consisting of a dry and wet season, could be discerned clearly.

34 These exhibit different sensitivities to changes in precipitation. Contrary to a previous published

35 report, no widespread decline in leaf area was detected across the entire extent of the Congolese

36 rainforests over the past two decades with the latest MODIS Collection 6 dataset. Long-term

37 precipitation decline did occur in some localized areas, but these had minimal impacts on leaf area,

38 as inferred from MODIS and MISR multi-angle observations.

39

40 _Keywords:_ leaf area, remote sensing, Congolese rainforests, phenology, long-term trends, MODIS,

41 MISR, DSCOVR EPIC

42

1. Introduction

Tropical rainforests play an essential role in modulating regional climate, surface energy partitioning and the Earth's carbon cycle (Chen et al. 2020; Cook et al. 2020). Understanding the spatial patterns and temporal variations and trends in the structure and functioning of rainforests, and the underlying mechanisms and their drivers, is crucial to gaining insights on how these biodiversly-rich and productive ecosystems will respond to future climate change, disturbances and human appropriation (Bi et al. 2015). The seasonal transition between wet and dry seasons is a distinct feature of tropical rainforests, which leads to intra-annual patterns of leaf flushing and abscission (Bi et al. 2015; Samanta et al. 2012). The growth-limiting impact of water deficit on rainforest during the dry season could be alleviated through deep roots and hydraulic redistribution (Oliveira et al. 2005; Pierret et al. 2016). However, a continued decline in leaf area and photosynthetic capacity attributed to long-term drying may alter forest composition and structure, such as large-scale tree mortality and dominance of drought-tolerant species (Adams et al. 2009; Fauset et al. 2012; Martínez-Vilalta and Lloret 2016).

Seasonal variations in the Amazonian rainforests has been an active research topic in recent years (Brando et al. 2010; Huete et al. 2006; Morton et al. 2014; Myneni et al. 2007). The community-consensual view is that higher greenness and leaf area appear during the sunlight-rich dry season in well-hydrated Amazonian rainforests (Bi et al. 2015; Brando et al. 2010; Huete et al. 2006; Myneni et al. 2007), even though this view has been questioned (Galvão et al. 2011; Morton et al. 2014). Science questions surrounding the functionality of Amazonian rainforests such as drought induced carbon sink variation and impacts of human interference are at the center of debates nowadays (Aragão et al. 2018; Brienen et al. 2015; Pires and Costa 2013; Yang et al. 2018b). The equatorial rainforests of Central Africa, the second largest and least disturbed of the biodiversly-rich and highly productive rainforests on Earth (Cook et al. 2020), have attracted less attention compared with its Amazonian counterpart.

The bimodal precipitation pattern (two wet and two dry seasons per year) in the Congo basin controlled by the migration of the tropical rain belt, is much different from that in the Amazon (Jiang et al. 2019; Nicholson 2018; Raghavendra et al. 2020; Sorí et al. 2017). For all vegetation types within the Congo Basin enhanced vegetation index (EVI) profiles were found to be highly

74   seasonal and strongly correlated to rainfall and to a lesser extent to light regimes (Gond et al.
75   2013). Two-band enhanced vegetation index (EVI2) from the geostationary Spinning Enhanced
76   Visible and Infrared Imager (SEVIRI) and polar-orbiting Moderate Resolution Imaging
77   Spectroradiometer (MODIS) also revealed similar bimodal seasonal pattern (Yan et al. 2016a). It
78   was found (Yan et al. 2017) that the spatial variation in wet season timing within the Congo Basin
79   exhibited distinct latitudinal gradients whereas the variation in the canopy greenness cycle timing
80   was relatively small. Analyses of MODIS EVI and solar-induced chlorophyll fluorescence (SIF)
81   and fraction of absorbed radiation from the Global Ozone Monitoring Experiment-2 (GOME-2)
82   suggest that an annual rainfall threshold of approximately 2000 mm yr^{-1} determines whether the
83   supply of seasonally redistributed subsurface water storage from the wet season can satisfy plant
84   water demands in the subsequent dry season; thus water availability exerts a first-order control on
85   photosynthetic seasonality in tropical forests (Guan et al. 2015; Ndehedehe et al. 2019).

86

87   Recent studies have also revealed a large-scale and long-term drying trend during the 1979 to
88   2010 period over the Congolese rainforests in central Africa (Jiang et al. 2019; Raghavendra et al.
89   2020; Zhou et al. 2014). This has been linked to a shift in tropical Walker circulation (Hua et al.
90   2018; Hua et al. 2016), intensifying thunderstorm activities (Raghavendra et al. 2018) and
91   Madden-Julian oscillation (Raghavendra et al. 2020). This drying was supposed to have led to a
92   widespread loss in greenness of Congolese forests during 2000 to 2012 as they were claimed to be
93   more sensitive and less resilient to climate change as compared to its Amazonian counterpart
94   (Hirota et al. 2011; Jiang et al. 2019; Zhou et al. 2014) . On the other hand, some recent studies
95   based on latest versions of satellite data reported no significant browning signals during the 2000
96   to 2017 period (Chen et al. 2019; Piao et al. 2020). As such, the question of greening or browning
97   of Congolese rainforests over the past 20 years is still unclear and in debate, especially in the
98   context of increasing drying durations and from the perspective of biophysical parameters.
99   Moreover, a drying climate over the past two decades has been associated with changes in forest
100 composition, leaf phenology and community-level functional traits in tropical forests (Aguirre-
101 Gutiérrez et al. 2020), which requires further explorations.

102

103 In addition to climatic factors mentioned above, degradational transitions in land cover and
104 agricultural expansion also drive the vegetation dynamics in rainforests (Costa et al. 2007). Since

105 the Congolese rainforests are less disturbed by human activities compared with other equatorial

106 forests (Cook et al. 2020), the climatic influence is our main focus. This study is focused on

107 exploring the intra-annual seasonality and its controls, inter-annual variability and long-term

108 trends in leaf area of the Congolese rainforests. More specifically, our primary objectives are to (*i*)

109 document seasonal variation in leaf area of Congolese rainforests and how do seasonal patterns

110 vary latitudinally within this large region; (*ii*) estimate the sensitivity of leaf area to changes in

111 precipitation for different regions and seasonal cycles; (*iii*) analyze long-term trends in leaf area;

112 and (*iv*) assess impact of long-term drying on leaf area and leaf optics. Multiple remote sensing

113 datasets and vegetation proxy metrics are analyzed to achieve our objectives.

114

115   Monitoring of dense vegetation such as equatorial rainforests represents one of the most

116 complicated case in optical remote sensing because reflection of solar radiation saturates and

117 becomes weakly sensitive to vegetation changes. At the same time, the satellite data are strongly

118 influenced by changing sun-sensor geometry. This makes it difficult to discriminate between

119 vegetation changes and sun-sensor geometry effects. As such, the above-mentioned leaf area

120 seasonal variation and long-term greening/browning trends revealed by single-viewing remotely

121 sensed datasets require more evidence. Our secondary objective is to demonstrate value of multi-

122 angle observations to unambiguously detect changes in properties of dense equatorial forests.

123

124 **2. Materials and Methods**

125

126 **2.1 Datasets**

127   Various variables from several independent satellite sensors over the Congo basin were

128 analyzed in this research. These include leaf area index (LAI), normalized difference vegetation

129 index (NDVI) (Rouse et al. 1974), EVI (Liu and Huete 1995), land cover maps, land surface

130 temperature (LST) and evapotranspiration (ET) from MODIS. Additionally, the following datasets

131 were also utilized in this research: precipitation from Tropical Rainfall Measuring Mission

132 (TRMM), photosynthetically active radiation (PAR) from Clouds and Earth's Radiant Energy

133 System (CERES), surface bidirectional reflectance factor (BRF) and directional hemispherical

134 reflectance (DHR) from Multi-angle Imaging SpectroRadiometer (MISR) on the Terra platform

135 and BRF from Earth Polychromatic Imaging Camera (EPIC) on Deep Space Climate Observatory

136 (DSCOVR). Table 1 shows datasets used in this study.

137

2.1.1. MODIS data

139 The Terra and Aqua MODIS Collection 6 (C6) 8-day composite LAI products (MOD15A2H

140 and MYD15A2H) for the period of February 2000 to December 2019 were used in this study. The

141 data are at 8-day temporal frequency and projected on a 500-m sinusoidal grid. The C6 MODIS

142 LAI product correctly accommodates structural and phenological variability in all biome types and

143 agree with ground truth data within root mean square error (RMSE) of 0.66 LAI (Yan et al. 2016b;

144 Yan et al. 2016c).

145

146 C6 Terra MODIS monthly NDVI and EVI products (MOD13C2) from February 2000 to

147 December 2019 were also used as radiometric measures of vegetation greenness. The NDVI is a

148 vegetation index widely used in many studies of vegetation dynamic. It is calculated as the

149 difference between BRFs at near-infrared (NIR) and red spectral bands normalized by their sum.

150 The EVI is calculated as the difference between BRFs at NIR and red spectral bands normalized

151 by a linear combination of BRFs at blue, red and NIR bands. It was found especially useful for

152 monitoring vegetation in high biomass tropical broadleaf forests (Brando et al. 2010; Xu et al.

153 2011; Zhou et al. 2014). The C6 MOD13C2 product is projected on a 0.05° geographic Climate

154 Modelling Grid (CMG) (Huete et al. 2002). In addition, monthly gridded Collection 5 (C5)

155 MODIS NDVI/EVI product (MODVI) from February 2000 to December 2012 in CMG 1°

156 resolution was also used in our study for comparisons.

157

158 C6 Terra and Aqua MODIS land cover product (MCD12C1) from 2001 to 2019 at yearly

159 intervals and at a 0.05° spatial resolution was used to identify our study area. Maps of several

160 classification schemes are available in the MCD12C1 dataset (Friedl et al. 2002). The map of LAI

161 classification scheme was adopted in this research (Supplementary Information Figure S1).

162

163 Daytime LST from C6 Aqua MODIS (MYD11C3) for the period July 2002 to December 2019

164 was used to quantify temperature variations related to changes in leaf area and other climate

165 variables. MYD11C3 measures the temperature of Earth's surface thermal emission at local time

166 ~13:30, which is believed to provide the largest LST contrast between vegetated and non-vegetated
167 surfaces compared to other MODIS LST measurements. Monthly LST values from the MYD11C3
168 product are derived by compositing and averaging values from the corresponding month of
169 MYD11C1 daily files, and projected on a 0.05° CMG grid (Wan 2014).
170
171 The Terra MODIS C6 8-day composite evapotranspiration product (MOD16A2) projected on
172 a 500-m sinusoidal grid from January 2000 to December 2019 was used to quantify climatic water
173 deficit variations. The algorithm used to generate MOD16A2 is based on the logic of the Penman-
174 Monteith equation, which includes inputs of daily meteorological reanalysis data along with other
175 MODIS products such as vegetation property dynamics, albedo, and land cover (Mu et al. 2007;
176 Mu et al. 2011).
177

2.1.2. TRMM Precipitation and CERES PAR Fluxes

179 Monthly precipitation data from the TRMM (3B43 version 7) at 0.25° spatial resolution for
180 the period January 2000 to December 2019 was used in this study. The 3B43 version 7 TRMM
181 data provides the best-estimate precipitation rate and root-mean-square precipitation-error
182 estimates by combining four independent precipitation fields (Huffman et al. 2007). Monthly at-
183 surface all-sky downward PAR, calculated by summarizing direct and diffuse PAR fluxes from
184 CERES (SYN1deg_L3 product) at 1° resolution for the period of March 2000 to November 2019
185 was used (Rutan et al. 2015).
186

2.1.3. Terra MISR and DSCOVR EPIC data

188 Level 2 land surface and aerosol products from MISR (version 3) for the period of January
189 2000 to December 2019 were used in this study. The MISR sensor views the Earth's surface with
190 nine cameras simultaneously and enables direct measurements of angular variation of forest
191 reflected radiation over a wide range of the phase angle that the single-viewing sensors (e.g., Terra
192 and Aqua MODIS) can provide only in very limited cases (Bi et al. 2015; Song et al. 2018). MISR
193 has a ground track repeat cycle every 16 days and achieves global coverage every 9 days. The
194 surface reflectances, DHR and BRF, are at 1.1 km spatial resolution. The aerosol optical depth
195 (AOD) is available at 4.4 km spatial resolution. The surface and aerosol products are projected on

196   Space Oblique Mercator (SOM) projection, in which the reference meridian nominally follows the
197   spacecraft ground track. The land surface product provides BRF at nine MISR view angles (nadir,
198   $\pm 26.1°$, $\pm 45.6°$, $\pm 60.0°$ and $\pm 70.5°$) in four spectral bands (446, 558, 672, and 866 nm). The MISR
199   view directions form "view" lines on the polar plane (Supplementary Information Figure S2). Each
200   view line sees a certain part of the MISR 360 km swath.

201

202   Level 2 Multi-Angle Implementation of Atmospheric Correction (MAIAC) surface BRF
203   retrieved from DSCOVR EPIC observations from 2016 to 2019 was also used. The EPIC
204   instrument provides imageries in near backscattering directions with the phase angle between $4°$
205   and $12°$ at ten ultra-violet to NIR narrow spectral bands. This feature complements MISR
206   observations since it extends MISR angular sampling to the near backscattering directions. The
207   MAIAC BRF are available at four spectral bands; they are 443, 551, 680 and 780 nm. Data are
208   projected on a 10-km sinusoidal grid and available at 65 to 110 min temporal frequency.

209

2.2. Data processing

211   This study was focused on structurally intact and undisturbed region of Congolese tropical
212   moist broadleaf forests in Central Africa ($5°N$-$6°S$, $14°E$-$31°E$), which were defined as a region
213   with no changes in land cover type during the 2000 to 2019 period. First, evergreen broadleaf
214   forest pixels in the LAI classification scheme at $0.05°$ resolution for which no land use/cover
215   change was detected during the 2000 to 2019 period were selected. Second, the binary $0.05°$
216   evergreen broadleaf forest images were spatially aggregated into a $0.25°$ coarser resolution map to
217   match the spatial resolution of rainfall TRMM dataset. Pixels at $0.25°$ resolution were labeled as
218   rainforest only if at least 80% of its $0.05°$ sub-pixels (i.e., 20 in 25 sub-pixels) were forested. Third,
219   those isolated pixels in the Congolese forest border were removed at $0.25°$ mask map to minimize
220   human impact. The 1,653 pixels at $0.25°$ resolution identified by this procedure were considered
221   as structurally intact and undisturbed forests.

222

223   All vegetation and climate variables were selected using flags indicating highest retrieval
224   quality. The 8-day 500 m LAI products from Terra (MOD15A2H) and Aqua (MYD15A2H)
225   MODIS sensors were used to generate monthly average LAI values. The cloud contaminated
226   pixels were removed. Only the best quality LAI values generated using main algorithm were used

227   in our analyses. The monthly LAIs were then spatially aggregated onto a 0.05° CMG grid (Chen
228   et al. 2019). The evapotranspiration data used in our study was generated by selecting best-quality
229   retrievals in the MODIS C6 ET product first and then degraded to 0.05° CMG monthly composites
230   following the same procedure used to obtain LAI dataset. The LAI and NDVI/EVI were further
231   refined by removing low quality data by consulting NDVI/EVI quality assurance (QA) flags. We
232   selected highest quality LST based on LST QA. The LAI, NDVI/EVI, ET and LST datasets over
233   intact and undisturbed region of the Congolese forests were then spatially aggregated to 0.25°
234   resolution. During the process of spatial aggregation, only pixel whose sub-pixels are all valid was
235   retained. Climatic water deficit (CWD) was calculated as the difference between potential
236   evapotranspiration and actual evapotranspiration from the ET dataset. Nearest neighbor
237   interpolation was adopted to resample data to 0.25° for the C5 NDVI/EVI and CERES PAR dataset
238   at a spatial resolution coarser than 0.25°.

239

240   The MISR surface BRF and DHR were first refined by removing pixels with AOD over 0.3.
241   EPIC images at local solar time around 10:30 am were used in our analyses, which were also
242   refined by removing pixels with AOD over 0.3. MISR and EPIC datasets were further re-projected
243   to 0.01° and 0.1° CMG grids, respectively. We expressed BRF and DHR values in a coordinate
244   system with the polar axis pointed towards the Sun. The view zenith angle in this "sun-tracking"
245   coordinates was given by the phase angle, γ, i.e. the angle between the directions to the sun and
246   sensor and calculated as

247

$$\gamma = \mathrm{acos}[\cos SZA \cos VZA + \sin SZA \sin VZA \cos(SAA - VAA)] \tag{1}$$

248

249   where SZA, VZA, SAA, VAA are solar zenith angle, view zenith angle, solar azimuthal angle and
250   view azimuthal angles (Bi et al. 2015). We assigned the sign "plus" to the phase angle if the
251   direction to the MISR sensor approached the direction to sun from North, and "minus" otherwise
252   (Supplementary Information Figure S2). In our sun-tracking coordinate system, the MISR BRF
253   was a function of SZA, phase angle and MISR view line, the latter specified by VZA of the MISR
254   nadir camera.

255

256   Monthly BRFs and DHRs accumulated over the 20-year period (2000 to 2019) were used to

257   analyze seasonal variation of forest canopy reflectance. For each month, a median BRF value at

258   each phase angle was calculated using all 20-year (2000 to 2019) valid observations of a given

259   pixel in our study area. Histograms of valid MISR spectral DHR at each SZA accumulated over

260   the 20-year period (2000 to 2019) were calculated for each pixel. The most probable values were

261   used to represent spectral DHR of regions as a function of SZA. For analysis of interannual

262   changes, we used median BRFs over the period of 2000-2002 and 2017-2019 to represent the start

263   and the end period, respectively.

264

265   **2.3. Interpretation of forest BRF**

266   Reflectance of dense vegetation such as the Congolese forests saturates and becomes weakly

267   sensitive to vegetation changes. At the same time, the satellite data are strongly influenced by

268   changing sun-sensor geometry. This makes it difficult to discriminate between vegetation changes

269   and effects of sun-sensor geometry. This section provides an overview of a new approach to detect

270   changed in properties of dense vegetation using angular distribution of forest reflected radiation

271   as a source of diagnostic information. This methodology will be used in Section 3.1 and Section

272   3.4 to corroborate seasonal and long-term variation in leaf area.

273

274   In the case of vegetation canopies with a dark background or sufficiently dense vegetation

275   where the impact of the canopy background is negligible, the BRF can be approximated as

276   (Knyazikhin et al. 2013):

277

$$\text{BRF}_\lambda(\Omega_0,\Omega) = \frac{\rho(\Omega_0,\Omega)i_0}{1-p} \times \frac{\omega_\lambda(1-p)}{1-p\omega_\lambda} \qquad (2)$$

278

279   The first factor on the right-hand side of Eq (2), $\rho(\Omega_0,\Omega)i_0/(1-p)$, is the Directional Area

280   Scattering Factor (DASF), which describes the canopy BRF if the foliage does not absorb

281   radiation. The second factor, $\omega_\lambda(1-p)/(1-p\omega_\lambda)$, is the Canopy Scattering Coefficient (CSC),

282   i.e., the fraction of intercepted radiation that has been reflected from, or diffusively transmitted

283   through, the vegetation. Unlike canopy reflectance and transmittance, the CSC quantifies

284   scattering event per unit leaf surface and therefore conveys information about leaf optical

285 properties. Here $\Omega_0 \sim (SZA, SAA)$ and $\Omega \sim (VZA, VAA)$ are unit vectors directed from target to the

286 sun and sensor, respectively; i_0 is the canopy interceptance defined as the portion of photons from

287 the incident solar beam that collide with foliage elements for the first time. The symbol ρ

288 designates the directional escape probability, i.e., the probability by which a photon scattered by a

289 foliage element will exit the vegetation in the direction Ω through gaps. Spherical integration of

290 $\pi^{-1}\rho \cdot cos(VZA)$ results in $1 - p$, where p is the recollision probability, defined as the probability

291 that a photon scattered by a foliage element in the canopy will interact within the canopy again

292 (Yang et al. 2017). Finally, ω_λ is the wavelength dependent leaf albedo, i.e., the fraction of

293 radiation incident on a leaf surface that is reflected or transmitted (Huang et al. 2007; Knyazikhin

294 et al. 2011; Wang et al. 2003). We used Eq. (2) to interpret the BRF of Congolese forests. A short

295 summary of its key properties is given below.

296

297   The spectrally invariant DASF is a function of canopy geometrical properties, such as the tree

298 crown shape and size, spatial distribution of trees on the ground, and within-crown foliage

299 arrangement (Knyazikhin et al. 2013). Since our study is focused on structurally intact and

300 undisturbed region of the Congolese forests (i.e., no changes in forest geometry), only variation in

301 leaf area can cause variation in DASF. At a given SZA, DASF increases with LAI in all phase

302 angles. At a given LAI, the DASF exhibits a sharp increase as phase angle tends to zero and reaches

303 its maximum value in the retro-illumination direction. This phenomenon is known as the hot spot

304 effect. Increasing SZA with constant LAI results in an asymmetric transformation of the DASF,

305 i.e., increase in its magnitude in backscattering directions, and changes in the range of DASF

306 variations for positive and negative phase angles. This asymmetric transformation also can cause

307 the two DASF signatures to intersect. More details about the effects of changing SZA and LAI on

308 BRF can be found in (Bi et al. 2015).

309

310   The spectrally varying CSC is a function of the recollision probability and leaf optics. It

311 increases with the leaf albedo: the more the leaves scatter, the brighter the canopy. As the

312 recollision probability increases with LAI, an increase in LAI triggers an opposite tendency: more

313 photon-foliage interactions and consequently a higher chance for photon to be absorbed. This tends

314 to lower CSC. Such variations trigger a competing process: increase in LAI tends to darken the

315 vegetation while increase in leaf albedo suppresses it. Note that DASF increases with LAI. This

316 not only compensates for a decrease in the CSC but also makes the BRF an increasing function
317 with respect to leaf albedo and LAI.
318
319   The leaf albedo is close to unity, $\omega_\lambda \sim 1$ at weakly absorbing wavelengths such as NIR. In the
320 case of dense vegetation, the recollision probability saturates and become weakly sensitive to LAI.
321 In many instances, variation in LAI with leaf albedo unchanged cannot explain the magnitude of
322 observed variation in CSC under the reflectance saturation conditions. Leaf albedo becomes a key
323 parameter that controls changes in the CSC. A detailed mathematical analysis of variation in the
324 CSC when LAI and leaf albedo vary simultaneously can be found in (Samanta et al. 2012).
325
326   The leaf albedo is close to zero, $\omega_\lambda \sim 0$ at strongly absorbing wavelengths. The contribution of
327 multiple scattered photons to BRF and CSC is negligible. A decrease in LAI while holding leaf
328 optics constant necessarily causes a decrease in BRF. The lack of BRF decrease indicates an
329 increase in leaf albedo. Clearly this is also true for DHR, which is just hemispherically integrated
330 BRF. We will use this property to detect changes in leaf albedo.
331
332   We followed a methodology documented in (Marshak and Knyazikhin 2017; Song et al. 2018)
333 to approximate DASF. In this approach, the green and NIR wavelengths are used. Given the BRF
334 at these two wavelengths, the estimate DASF is as:
335

$$\text{DASF} = \frac{\text{BRF}_{\text{green}} \text{BRF}_{\text{NIR}}}{\text{BRF}_{\text{green}} - \beta(\text{BRF}_{\text{NIR}} - \text{BRF}_{\text{green}})}. \tag{3}$$

336
337 Here $\text{BRF}_{\text{green}}$ and BRF_{NIR} are BRF at green and NIR wavelengths, $\beta = (1 - \omega_{\text{NIR}})\omega_{\text{green}}/$
338 $(\omega_{\text{NIR}} - \omega_{\text{green}})$, and ω_{green} and ω_{NIR} stand for leaf albedo at green and NIR spectral bands.
339 DASF defined by Eq. (3) does not vary with variation in ω_{green} and ω_{nir} as long as canopy
340 structure remains unchanged. We used the leaf level albedo of the brightest leaf, whose values at
341 green and NIR spectral bands were $\omega_{555} = 0.472$, $\omega_{865} = 0.978$ for MISR and $\omega_{551} = 0.490$,
342 $\omega_{779} = 0.979$ for EPIC. These values were obtained from Lewis and Disney's approximation
343 (Lewis and Disney 2007) of the PROSPECT model (Féret et al. 2008) with the following
344 parameters: chlorophyll content of 16 μg cm^{-2}; equivalent water thickness of 0.005 cm^{-1}, and dry

345   matter content of 0.002 g cm^{-1}. It was shown that retrieval of DASF using this methodology is

346   weakly sensitive to the uncertainties in the spectral properties of the atmospheric optical depth

347   above the canopy, and the spectral CSC is very sensitive to the presence of chlorophyll in the scene

348   (Marshak and Knyazikhin 2017).

349

350   **2.4. Correlation and trends analysis**

351   Correlation of monthly average leaf area and the corresponding climatic variables (e.g.,

352   precipitation, PAR) was assessed using Pearson's correlation coefficient. Trends in seasonal

353   average variables (e.g., LAI) for the period of 2000 to 2012 and 2000 to 2019 were evaluated by

354   ordinary least square (OLS) regression test using noise-removed dataset, and the trends with P $\leq$

355   0.1 were considered as statistically significant in this study to make our results comparable with

356   those reported in (Zhou et al. 2014).

357

358   **3. Results**

359   **3.1. Seasonal variation of leaf area and leaf optics**

360   Monthly precipitation data over the Congolese forests show a bimodal variation that suggests

361   two wet and two dry seasons during the year. It varies between its maximum of about 219 mm in

362   October and the minimum of about 86 mm in January (Figure 1). The wet seasons occur in March-

363   April-May (MAM, wet season 1) and September-October-November (SON, wet season 2), while

364   dry season months are December-January-February (DJF, dry season 1) and June-July-August

365   (JJA, dry season 2) (Figure 1 and Supplementary Information Figure S3a). The PAR data exhibit

366   a quasi-bimodal pattern, although somewhat less distinctly: clear-cut variations from December to

367   October and a weak oscillation from October to December (Figure 1 and Supplementary

368   Information Figure S3). The sub-seasonal cycle 1 from December to May (dry season 1 and wet

369   season 1) shows less precipitation and more PAR, while cycle 2 from June to December has more

370   precipitation and less PAR (Figure 1 and Supplementary Information Figure S3). Monthly average

371   LAI and EPIC NIR BRF data over the Congolese forests also exhibit notable bimodal seasonal

372   variations, which follow the patterns of precipitation (Figure 1 and Supplementary Information

373   Figure S3a and b). LAI varies between its maximum of about 5.7 during the wet seasons and a dry

374   season minimum of about 4.6.

375   Congolese forests can be further divided into four phenological regions based on normalized
376   20-year mean monthly climatology of precipitation, PAR and LAI using a K-means clustering
377   method, which is an unsupervised measure to find similar features from multiple inputs (Celik
378   2009; Xu et al. 2015). We use the four-cluster partition in this study because clusters are big
379   enough to accumulate valid data for statistical analyses and their respective homogeneities are
380   preserved (Figure 2). Other numbers of clusters are also tested to find an optimal partitioning, and
381   all clusters were generally parallel to the Equator (Supplementary Information Figure S4), likely
382   because the seasonality of these forests is mainly controlled by the migration of the tropical rain
383   belt and variation of solar radiation along the latitude. Distinct seasonal patterns of climatic and
384   vegetation variables are clearly seen in all phenological regions across the Congo Basin (Figure
385   3). The amplitude of all variables tends to increase from region 1 (north) to region 3 (south)
386   between March and October, which makes the bimodality more distinct. The highland forest
387   (region 4) is characterized by lower LAI values and higher rainfall compared to its lowland
388   counterparts, which is typical of montane forests. The EPIC sensor likely sees different slopes of
389   the mountains; hence the NIR BRF is somewhat less synchronized with LAI compared to other
390   regions. We exclude this region from further analyses given its smaller areal extent and specific
391   character.
392
393   Spectrally invariant DASF is a function of canopy geometrical properties, such as the tree
394   crown shape and size, and leaf area density within the canopy. The DASF derived from MISR and
395   EPIC observations of selected regions during wet and dry seasons are different (Figure 4, left
396   Panels), showing a districting decrease in all directions from wet (October, November) to dry
397   (January) seasons. Such a downward shift in DASF can only result from a negative change in LAI
398   because other structural variables, such as tree crown shape and size do not vary seasonally in our
399   forests. BRF at NIR spectral band exhibits similar behavior: a decrease in reflected radiation in all
400   directions from October (November) to January (Supplementary Information Figure S5), which
401   suggests more green leaves during the wet season. The CSC shows an opposite tendency, i.e., a
402   positive increase between wet and dry seasons at all spectral bands (Figure 4, right panels). The
403   decline in LAI is one reason for the observed increase (Section 2.3). A change in leaf albedo is
404   another reason that can impact this coefficient (Section 2.3). Decrease in leaf albedo lowers the

405 CSC value whereas its increase results in the positive change of the CSC value. The question then
406 arises whether one can detect changes in the leaf albedo given changes in the CSC.

407

408   A reduction of leaf area tends to decrease forest canopy reflectance (BRF and consequently
409 DHR). At strongly absorbing red (672 nm) wavelength, however, the DHR has increased between
410 wet and dry seasons from 0.014 to about 0.024 in regions 1 and 2 and from 0.015 to 0.018 in region
411 3 (Figure 4, left panels). This increase in DHR with decreasing LAI necessarily indicates an
412 increase in leaf albedo (Section 2.3). This also takes place for strongly absorbing blue (446 nm)
413 and moderately absorbing green (551 nm) wavelengths: no decrease in DHR from wet to dry
414 season. This suggests an increase in leaf albedo at visible spectral bands. At NIR (866 nm)
415 wavelength, forest canopy reflectance and CSC show opposite tendencies, namely, BRF (and
416 DHR) decrease whereas CSC increases between wet and dry seasons. Similar tendencies were
417 documented for the Amazonian rainforests (Köhler et al. 2018) and for sufficiently dense broad-
418 and needleleaf forests in the USA (Knyazikhin et al. 2013). A decrease in LAI (and consequently,
419 the recollision probability) tends to increase the CSC (Section 2.3). Under saturation conditions,
420 however, the change in the recollision probability is negligible. The observed variation in CSC is
421 therefore likely due to a positive change in the leaf albedo.

422

423   The sensitivity analyses based on the PROSAIL model (Jacquemoud et al. 2009) suggest that
424 under saturation conditions (LAI>4), the scattering coefficient is nearly insensitive to variations in
425 LAI and SZA (Supplementary Information Figure S6, panels a and b). The observed changes in
426 the CSC between wet and dry seasons therefore are not due variation in LAI and SZA. In the
427 spectral interval between 450 nm and about 750 nm, chlorophyll is the dominant pigment that
428 absorbs radiation primarily in the blue and red regions of the spectrum, less in in the green and
429 essentially none in NIR. This feature makes the CSC sensitive to its concentration in the green and
430 flat in NIR spectral bands (Supplementary Information Figure S6, panel c). The chlorophyll
431 absorption spectrum declines rapidly with wavelength near the red spectral region and vanishes at
432 about 770 nm, resulting in a sharp jump in the spectrum of leaf albedo from its minimum to a
433 plateau around 800 nm. The magnitude of this plateau is controlled by the amount of dry matter.
434 This imparts sensitivity of the NIR CSC to the concentration of dry matter (Supplementary
435 Information Figure S6, plot d).

436   In summary, seasonal variation of leaf area in Congolese forests co-varies with the bimodal

437   precipitation pattern, with higher values during the wet seasons. The bimodal pattern is different

438   in the three identified regions, with its bimodality more distinct from the south to the north. The

439   canopy scattering coefficient exhibits an opposite tendency: its value increases from wet to dry

440   and decreases from dry to wet seasons. These variations can be linked to variation in the

441   concentrations of chlorophyll and/or dry matter in green leaves.

442

3.2. Sensitivity of leaf area to changes in precipitation

444   Pearson's correlation coefficients between monthly average precipitation, PAR and LAI for

445   the identified regions (Figure 2) and seasonal periods are shown in Table 2. With the exception of

446   region 3 and seasonal cycle 1, a significant positive correlation between precipitation and LAI is

447   observed. Moreover, the time series of 20-year monthly precipitation and LAI over the Congolese

448   forests are also significantly positively correlated (R=0.67, P<0.01, Supplementary Information

449   Figure S7). Such correlations between LAI and PAR (P<0.01) are found in regions 1 to 3 during

450   the cycle 2 (June through November) and in region 3 during the cycle 1 (December through May).

451   These variables are negatively correlated (P<0.1) in region 1 during cycle 1 (Table 2).

452

453   We estimate the sensitivity, ΔLAI/Δprecipitation, of monthly LAI to changes in precipitation

454   for different regions and seasonal cycles using the slopes of linear regressions. The overall

455   sensitivity of LAI to changes in precipitation varies between regions and depends on the seasonal

456   cycle. It tends to decrease from north to south for the full seasonal cycle (December to November)

457   (Figure 5a). The regions show weak variation of the sensitivity within seasonal cycles (cf. Figure

458   5b and 5c). LAI exhibits a stronger response to changes in the precipitation during the seasonal

459   cycle 1 (December to June). This difference is due to very different distributions of precipitation,

460   PAR and climatic water deficit during cycles 1 and 2 (Supplementary Information Figure S8).

461   More precipitation occurs in cycle 2 than in cycle 1, causing a higher climatic water deficit. Thus,

462   LAI in our forests is more sensitive to the changes in precipitation during cycle 1.

463

3.3. Long-term trends in leaf area

A widespread decline in Congolese rainforest greenness over the 2000-2012 period has been recently reported (Jiang et al. 2019; Raghavendra et al. 2020; Zhou et al. 2014). This result however was questioned, suggesting no significant browning signal in the 2000 to 2017 period (Chen et al. 2019; Piao et al. 2020). These contradictory results justify a re-examination of the long-term trend in greenness of the Congolese forests. Here, we reproduce linear trends in C5 EVI and precipitation in April-May-June for the 2000 to 2012 period as reported in (Zhou et al. 2014) and for an extended period of 2000 to 2019 first, and then generate linear trends in C6 EVI, NDVI and LAI for the same periods.

The MODIS C5 EVI declines over 98% of the study area, with 54% showing a significant negative trend (P<0.1) (Figure 6a). TRMM precipitation declines over 77% of the area with 13% indicating significant change with P<0.1 (Figure 6b). These results suggest decrease in rainfall and widespread decline in Congo rainforest greenness from 2000 to 2012. Note that "drying area" is reduced from 77% to 63% (13% to 5% with P<0.1) for the period of 2000 to 2019.

The widespread decline of Congo rainforest greenness in the 2000 to 2012 period has disappeared in the latest Collection 6 MODIS data (Figure 6, middle panels). Our re-analyses suggest declines in EVI, NDVI and LAI over 43% to 51% of the study area with only 2% to 5% showing significant negative trends (P<0.1). For the longer period (2000 to 2019), the browning areas have been reduced to 19%-42%, with a negative trends below 4% (P<0.1) (Figure 6, lower panels). The difference in the trends is attributable to Terra MODIS sensor degradation found in C5 data (Wang et al. 2012; Zhang et al. 2017).

The regional mean precipitation and PAR over 20 years do not show significant positive or negative trends for all seasons across the Congo basin because of strong interannual variability (Supplementary Information Figure S9). The regional mean LAI, however, increases by 0.0865 (P=0.0168) per decade during wet season 1 (March to May) from 2000 to 2019 (Supplementary Information Figure S9b), and the leaf area trends are also positive but not significant for the other wet or dry seasons (Supplementary Information Figure S9a, c, d).

3.4. Impact of drying trends on leaf area and leaf optics

Here we focus on a South-East part (0.5°N-2.5°S, 25.5°E-28.5°E) of our study area, where a significant precipitation decline is observed (Figures 7a and b), with the goal of understanding the impact of this event on changes in forest structure and leaf optics.

With the exception of NDVI in the dry season 2 (June to August), no significant decline or increase in trends in regional mean NDVI, EVI and LAI over the past two decades are detected. The time series of LAI and EVI are found to be strongly correlated with R=0.56 (P<0.01) in wet season 1 (MAM) and R=0.74 (P<0.01) in dry season 2 (JJA).

Next, we examine MISR BRFs at NIR (866 nm) spectral band over the region with significant drying happened during the early (2000-2002) and later (2017-2019) part of the 20-year observation period. Reflectance in April (wet season) and June (dry season) are under almost identical observation and illumination conditions (Figure 8 left panels). No significant differences in magnitude and shape of angular signatures of the reflected radiation at the beginning and the end of our observation period have been detected. Similarly, no changes in the canopy spectral coefficient at all MISR spectral bands are found. These findings suggest no changes in structure and leaf optics of the Congolese forests before and after the observed drying event. Thus we conclude, MODIS NDVI, EVI and LAI long-term records and MISR angular signatures of forest reflected radiation show no signs of long-term drying impact on structure and leaf optics of the Congolese forests.

4. Discussion

Tropical rainforests play an essential role in modulating regional climate, surface energy balance and the Earth's carbon cycle (Chen et al. 2020; Cook et al. 2020). Understanding the seasonal and long-term variations in the structure and function of these ecosystems is crucial to prognosing their response to climate change (Bi et al. 2015). The equatorial central African rainforests, the second-largest on Earth after the Amazonian rainforests, is still lacking systematic analyses of its phenological behavior and interannual variation. The purpose of this study is to analyze seasonal changes and long-term trends in leaf area in intact and undisturbed regions of the

525 Congolese rainforests (Supplementary Information Figure S1) using remote sensing data from the

526 past two decades. We focus on the analysis on three regions identified with normalized 20-year

527 mean monthly climatology of precipitation, PAR and LAI by using a K-means clustering

528 algorithm, an unsupervised measure to find similar features from multiple inputs (Figure 2). This

529 clustering technique also localizes a highland region in the southeast part (Region 4 in Figure 2)

530 that represents a montane ecosystem.

531

532 Monthly precipitation data from TRMM show a bimodal variation over the Congolese

533 rainforest, suggesting two dry (December-January-February and June-July-August) and two wet

534 (September-October-November and March-April-May) seasons (Figure 3). This is consistent with

535 other precipitation datasets, such as Global Precipitation Climatology Centre (GPCC), Global

536 Precipitation Climatology Project (GPCP) and Climatic Research Unit (CRU) (Jiang et al. 2019;

537 Raghavendra et al. 2020; Sorí et al. 2017). Monthly average LAI from MODIS and forest canopy

538 reflectance from EPIC follow seasonal patterns of precipitation, with higher values during the wet

539 seasons (Figure 3). The PAR incident on the forest canopy also exhibits a bimodal pattern,

540 although somewhat less distinct: clear-cut variations from December to October and a weaker

541 oscillation from October to December. Sub-seasonal cycle from December to May shows less

542 precipitation and more PAR, while the cycle from June to December has more precipitation and

543 less PAR (Figure 3). The bimodal patterns vary latitudinally with the amplitude increasing from

544 North to South (Figure 3).

545

546 The MODIS LAI values used in this research are mostly retrieved under the condition of

547 reflectance saturation. The seasonality of satellite data-based LAI may therefore result from a

548 decreased retrieval accuracy and/or variation in sun-satellite sensor geometry (Galvão et al. 2011;

549 Morton et al. 2014). We develop a new approach that allows us to unambiguously detect changes

550 in properties of the Congolese rainforest using angular variation of forest BRF as a source of

551 diagnostic information. This methodology is applied to obtained independent observational

552 evidence from MISR and EPIC data in support of the validity of the satellite derived seasonal

553 variation in leaf area. Angular variations of forest DASF and canopy reflectance observed by the

554 MISR and EPIC sensors clearly show seasonal increases and decreases in the amount of radiation

555 reflected by the Congolese forests in all directions simultaneously (Figure 4; Supplementary

556 Information Figure S5). Such changes can only be attributed to corresponding seasonal increases

557 and decreases of LAI. This corroborates the seasonal behavior of leaf area derived from the

558 MODIS observations. We also find that the canopy scattering coefficient exhibits an opposite

559 tendency: its value increases from wet to dry and decreases from dry to wet seasons in the

560 Congolese rainforests (Figure 4, right panels). Similar tendencies were also found in Amazonian

561 rainforests (Köhler et al. 2018). Such variation can be linked to variation in the concentrations of

562 chlorophyll and/or dry matter in green leaves (Supplementary Information Figure S6). In

563 summary, our approach based on exploiting angular variation of forest reflected radiation as a

564 source of diagnostic information, rooted in physics of radiative transfer, allows us to

565 unambiguously detect changes in canopy structure and leaf optics. This undoubtedly offers the

566 benefit of greater reliability of our conclusion.

567

568   A significant positive correlation between precipitation and LAI is observed for our study area

569 and seasonal cycles (Table 2). The time series of 20-year monthly precipitation and LAI over the

570 Congolese forests are significantly positively correlated (R=0.67, P<0.01, Figure S7). Whereas

571 LAI and precipitation are always positively correlated, correlation between LAI and PAR can be

572 both negative as during cycle 1 in regions 1 and 2 and positive as in cycle 2 (Table 2). These

573 findings suggest that the observed seasonality of LAI is mainly controlled by precipitation in the

574 Congolese rainforests (Gond et al. 2013; Yan et al. 2016a), as contrast to its Amazonian

575 counterpart, where LAI is positive correlated with PAR (Bi et al. 2015; Brando et al. 2010; Huete

576 et al. 2006; Myneni et al. 2007). Abundant annual precipitation (2,332 mm yr^{-1}) creates a well-

577 hydrated environmental condition in the Amazonian rainforests (Yang et al. 2018a), thus the water

578 is not a main limitation and higher leaf area appears during the sunlight-rich dry season. A decrease

579 in annual precipitation (1,775 mm yr^{-1}) makes the leaf flushing and photosynthesis in the

580 Congolese rainforests more dependent on water supply, especially in dry season when the monthly

581 precipitation can fall below 90 mm (Figure 1). Less solar radiation during the dry season (Figure1

582 and Supplementary Information Figure S3) may lead to lower leaf area in the Congolese

583 rainforests. This, however, can only explain LAI decrease in dry season 2 (JJA). In addition, a

584 low-level cloudiness developing during the dry season 2 causes high quality of light that sustain a

585 more efficient photosynthesis (Mercado et al. 2009; Philippon et al. 2019), which should benefits

586 leaf area growing. Hence, water supply is believed as the main limitation for seasonal leaf area

587 variation. From the ecological perspective, the difference in the total annual precipitation and its
588 diverse intra-annual variability strongly influence phenological behavior of rainforests and other
589 vegetation types in the tropical regions (Ndehedehe et al. 2019; Yan et al. 2017).
590

591   Distinct spatiotemporal dependence of leaf area sensitivity to the seasonal variation in
592 precipitation is observed in the Congo basin. The sensitivity of LAI to changes in precipitation
593 tends to decrease from north to south for the full seasonal cycle (December to November, Figure
594 5a). The phenological regions (Figure 2) show weak variations of the sensitivity within a seasonal
595 cycle (cf. Figure 5b and 5c). LAI exhibits a stronger response to changes in precipitation from
596 December to June compared to the second seasonal cycle (June to November). This difference is
597 attributed to very different distributions of precipitation, PAR and climatic water deficit during the
598 two seasonal cycles (Supplementary Information Figure S8). Note that only very few factors were
599 accounted for in our analyses. Further analyses of combined effects of precipitation, PAR, and
600 other factors are needed to obtain a comprehensive insight into the causes of leaf area seasonal
601 variation. Besides, a better understanding of the phenological response of Congolese rainforests
602 depends on further *in situ* studies as satellite data can only complement but not substitute field
603 data.
604

605   A widespread decline in Congolese rainforest greenness over the 2000-2012 period has been
606 recently reported (Jiang et al. 2019; Raghavendra et al. 2020; Zhou et al. 2014). This result
607 however was questioned, suggesting no significant browning signal in the 2000 to 2017 period
608 (Chen et al. 2019; Piao et al. 2020). These contradictory results justify a re-examination of the
609 long-term trend in greenness of the Congolese forests.
610

611   We reproduce their result using the same Terra MODIS C5 EVI data (Figure 6, upper panels),
612 which is then compared to that from the latest MODIS C6 EVI dataset. We find that the widespread
613 decline of Congo rainforest greenness disappear in the latest C6 MODIS data (Figure 6, middle
614 and lower panels): only 2% to 3% of the forests show significant negative trends in EVI, NDVI
615 and LAI (P<0.1) compared to 54% (P<0.1) decline in EVI reported in (Zhou et al. 2014). The
616 difference in the trends detected by C5 and C6 EVIs is attributed to the Terra MODIS sensor
617 degradation for the period after 2007 (Lyapustin et al. 2014; Wang et al. 2012; Zhang et al. 2017).

618   Moreover, a significant increase in total aerosols over the Congolese rainforests within the last
619   decade has been detected (Moparthy et al. 2019). This can amplify the apparent long-term trends
620   of canopy greenness these changes in aerosol loads are not correctly taken into account. C6 data
621   reprocessing has significantly alleviated these problems (Detsch et al. 2016; Zhang et al. 2017)
622   and made the result more credible.

623

624   A significant precipitation decline has been observed in the South-East part of our study area
625   (Figures 7a and b). However, no significant decline or increase in trends in regional mean NDVI,
626   EVI and LAI over the past two decades are detected (Figures 7c and d). The time series of LAI
627   and EVI are found to be strongly correlated with R=0.56 (P<0.01) during wet (March-April-May)
628   and R=0.74 (P<0.01) during dry (June-July-August) seasons. We also find no significant
629   differences in magnitude and shape of angular distribution of forest reflected radiation and leaf
630   optics at the beginning and the end of our observation period (Figure 8). Thus, MODIS NDVI,
631   EVI and LAI long-term records and MISR angular signatures of forest reflected radiation show no
632   signs of drying impact on structure and leaf optics even in the South-East part of the Congolese
633   forests where a significant drying is observed.

634

635   Long-term drying does not induce vegetation degradation, and possible explanations for the
636   neutral response of leaf area to the declines in precipitations at the seasonal and inter-annual scales
637   could be given as follows. First, the decrease in monthly precipitation under a long-term drying
638   condition is much smaller compared to a wet-to-dry precipitation amplitude of about 219 mm to
639   86 mm (Figure 1), which still can satisfy plant water demands. Dry frequency is not high enough
640   to suppress compensation of water supply from other months or seasons, allowing the forest to
641   endure precipitation deficit. Second, decades of long-term drying in the Congolese rainforests may
642   result in more drought-adapted species compared with other tropical forests, and this adaptive
643   mechanisms by utilization of soil water reserves can tolerate water deficit short-time events (Asefi-
644   Najafabady and Saatchi 2013; Borchert 1998). Third, suitable climate conditions—slight
645   temperature increase and climatic water deficit decline (Supplementary Information Figure S10),
646   may benefit the growth of vegetation (Li et al. 2019) and in turn offset the negative impact from
647   precipitation decline. More comprehensive explorations, such as model-based study, on this debate
648   are still needed in the future investigation to get a better understanding.

5. Conclusion

This study comprehensively evaluated the seasonality and long-term trends of leaf area in Congolese forests with multiple remotely sensed datasets. We found that the seasonal variations of leaf area from MODIS data co-vary with the bimodal precipitation pattern, with higher values during the wet season, and the bimodal patterns vary latitudinally within this large region. Angular reflectance signatures derived from MISR and EPIC data further corroborated this seasonal behavior of leaf area. Two sub-seasonal cycles, each consisting of a dry and wet season, exhibited different leaf area sensitivities to changes in precipitation. No widespread decline in leaf area was detected across the Congolese rainforest over the past two decades with the latest MODIS C6 dataset. Long-term drying did happen in some local areas of Congolese forests; however, those had minimal impacts on leaf area detected from MODIS and MISR observations.

Acknowledgment

References

Adams, H.D., Guardiola-Claramonte, M., Barron-Gafford, G.A., Villegas, J.C., Breshears, D.D., Zou, C.B., Troch, P.A., & Huxman, T.E. (2009). Temperature sensitivity of drought-induced tree mortality portends increased regional die-off under global-change-type drought. *Proceedings of the National Academy of Sciences, 106*, 7063-7066

Aguirre-Gutiérrez, J., Malhi, Y., Lewis, S.L., Fauset, S., Adu-Bredu, S., Affum-Baffoe, K., Baker, T.R., Gvozdevaite, A., Hubau, W., Moore, S., Peprah, T., Ziemińska, K., Phillips, O.L., & Oliveras, I. (2020). Long-term droughts may drive drier tropical forests towards increased functional, taxonomic and phylogenetic homogeneity. *Nature Communications, 11*, 3346

Aragão, L.E.O.C., Anderson, L.O., Fonseca, M.G., Rosan, T.M., Vedovato, L.B., Wagner, F.H., Silva, C.V.J., Silva Junior, C.H.L., Arai, E., Aguiar, A.P., Barlow, J., Berenguer, E., Deeter, M.N., Domingues, L.G., Gatti, L., Gloor, M., Malhi, Y., Marengo, J.A., Miller, J.B., Phillips, O.L., & Saatchi, S. (2018). 21st Century drought-related fires counteract the decline of Amazon deforestation carbon emissions. *Nature Communications, 9*, 536

Asefi-Najafabady, S., & Saatchi, S. (2013). Response of African humid tropical forests to recent rainfall anomalies. *Philosophical Transactions of the Royal Society B: Biological Sciences, 368*, 20120306

Bi, J., Knyazikhin, Y., Choi, S., Park, T., Barichivich, J., Ciais, P., Fu, R., Ganguly, S., Hall, F., Hilker, T., Huete, A., Jones, M., Kimball, J., Lyapustin, A.I., Mottus, M., Nemani, R.R., Piao, S., Poulter, B., Saleska, S.R., Saatchi, S.S., Xu, L., Zhou, L., & Myneni, R.B. (2015). Sunlight mediated seasonality in canopy structure and photosynthetic activity of Amazonian rainforests. *Environmental Research Letters, 10*

Borchert, R. (1998). Responses of Tropical Trees to Rainfall Seasonality and its Long-Term Changes. *Climatic Change, 39*, 381-393

Brando, P.M., Goetz, S.J., Baccini, A., Nepstad, D.C., Beck, P.S.A., & Christman, M.C. (2010). Seasonal and interannual variability of climate and vegetation indices across the Amazon. *Proceedings of the National Academy of Sciences, 107*, 14685-14690

Brienen, R.J.W., Phillips, O.L., Feldpausch, T.R., Gloor, E., Baker, T.R., Lloyd, J., Lopez-Gonzalez, G., Monteagudo-Mendoza, A., Malhi, Y., Lewis, S.L., Vásquez Martinez, R., Alexiades, M., Álvarez Dávila, E., Alvarez-Loayza, P., Andrade, A., Aragão, L.E.O.C., Araujo-Murakami, A., Arets, E.J.M.M., Arroyo, L., Aymard C, G.A., Bánki, O.S., Baraloto, C., Barroso, J., Bonal, D., Boot, R.G.A., Camargo, J.L.C., Castilho, C.V., Chama, V., Chao, K.J., Chave, J., Comiskey, J.A., Cornejo Valverde, F., da Costa, L., de Oliveira, E.A., Di Fiore, A., Erwin, T.L., Fauset, S., Forsthofer, M., Galbraith, D.R., Grahame, E.S., Groot, N., Hérault, B., Higuchi, N., Honorio Coronado, E.N., Keeling, H., Killeen, T.J., Laurance, W.F., Laurance, S., Licona, J., Magnussen, W.E., Marimon, B.S., Marimon-Junior, B.H., Mendoza, C., Neill, D.A., Nogueira, E.M., Núñez, P., Pallqui Camacho, N.C., Parada, A., Pardo-Molina, G., Peacock, J., Peña-Claros, M., Pickavance, G.C., Pitman, N.C.A., Poorter, L., Prieto, A., Quesada, C.A., Ramírez, F., Ramírez-Angulo, H., Restrepo, Z., Roopsind, A., Rudas, A., Salomão, R.P., Schwarz, M., Silva, N., Silva-Espejo, J.E., Silveira, M., Stropp, J., Talbot, J., ter Steege, H., Teran-Aguilar, J., Terborgh, J., Thomas-Caesar, R., Toledo, M., Torello-Raventos, M., Umetsu, R.K., van der Heijden, G.M.F., van der Hout, P., Guimarães Vieira, I.C., Vieira, S.A., Vilanova, E., Vos, V.A., & Zagt, R.J. (2015). Long-term decline of the Amazon carbon sink. *Nature, 519*, 344-348

Celik, T. (2009). Unsupervised Change Detection in Satellite Images Using Principal Component Analysis and k-Means Clustering. *IEEE Geoscience and Remote Sensing Letters, 6*, 772-776

Chen, C., Li, D., Li, Y., Piao, S., Wang, X., Huang, M., Gentine, P., Nemani, R.R., & Myneni, R.B. (2020). Biophysical impacts of Earth greening largely controlled by aerodynamic resistance. *Science Advances, 6*, eabb1981

Chen, C., Park, T., Wang, X., Piao, S., Xu, B., Chaturvedi, R.K., Fuchs, R., Brovkin, V., Ciais, P., Fensholt, R., Tømmervik, H., Bala, G., Zhu, Z., Nemani, R.R., & Myneni, R.B. (2019). China and India lead in greening of the world through land-use management. *Nature Sustainability, 2*, 122-129

Cook, K.H., Liu, Y., & Vizy, E.K. (2020). Congo Basin drying associated with poleward shifts of the African thermal lows. *Climate Dynamics, 54*, 863-883

721 Costa, M.H., Yanagi, S.N.M., Souza, P.J.O.P., Ribeiro, A., & Rocha, E.J.P. (2007). Climate change
722 in Amazonia caused by soybean cropland expansion, as compared to caused by pastureland
723 expansion. *Geophysical Research Letters, 34*

724 Detsch, F., Insa, O., Appelhans, T., & Nauss, T. (2016). A Comparative Study of Cross-Product
725 NDVI Dynamics in the Kilimanjaro Region—A Matter of Sensor, Degradation Calibration, and
726 Significance. *Remote Sensing, 8*

727 Fauset, S., Baker, T.R., Lewis, S.L., Feldpausch, T.R., Affum-Baffoe, K., Foli, E.G., Hamer, K.C.,
728 & Swaine, M.D. (2012). Drought-induced shifts in the floristic and functional composition of
729 tropical forests in Ghana. *Ecology Letters, 15*, 1120-1129

730 Féret, J.B., Francois, C., Asner, G.P., Gitelson, A.A., Martin, R.E., Bidel, L.P.R., Ustin, S.L., le
731 Maire, G., & Jacquemoud, S. (2008). PROSPECT-4 and 5: Advances in the leaf optical properties
732 model separating photosynthetic pigments. *Remote Sensing of Environment, 112*, 3030-3043

733 Friedl, M.A., McIver, D.K., Hodges, J.C.F., Zhang, X.Y., Muchoney, D., Strahler, A.H., Woodcock,
734 C.E., Gopal, S., Schneider, A., Cooper, A., Baccini, A., Gao, F., & Schaaf, C. (2002). Global land
735 cover mapping from MODIS: algorithms and early results. *Remote Sensing of Environment, 83*,
736 287-302

737 Galvão, L.S., dos Santos, J.R., Roberts, D.A., Breunig, F.M., Toomey, M., & de Moura, Y.M.
738 (2011). On intra-annual EVI variability in the dry season of tropical forest: A case study with
739 MODIS and hyperspectral data. *Remote Sensing of Environment, 115*, 2350-2359

740 Gond, V., Fayolle, A., Pennec, A., Cornu, G., Mayaux, P., Camberlin, P., Doumenge, C., Fauvet,
741 N., & Gourlet-Fleury, S. (2013). Vegetation structure and greenness in Central Africa from Modis
742 multi-temporal data. *Philosophical Transactions of the Royal Society B: Biological Sciences, 368*,
743 20120309

744 Guan, K., Pan, M., Li, H., Wolf, A., Wu, J., Medvigy, D., Caylor, K.K., Sheffield, J., Wood, E.F.,
745 Malhi, Y., Liang, M., Kimball, J.S., Saleska, Scott R., Berry, J., Joiner, J., & Lyapustin, A.I. (2015).
746 Photosynthetic seasonality of global tropical forests constrained by hydroclimate. *Nature
747 Geoscience, 8*, 284-289

748 Hirota, M., Holmgren, M., Van Nes, E.H., & Scheffer, M. (2011). Global Resilience of Tropical
749 Forest and Savanna to Critical Transitions. *Science, 334*, 232-235

750 Hua, W., Zhou, L., Chen, H., Nicholson, S.E., Jiang, Y., & Raghavendra, A. (2018). Understanding
751 the Central Equatorial African long-term drought using AMIP-type simulations. *Climate Dynamics,
752 50*, 1115-1128

753 Hua, W., Zhou, L., Chen, H., Nicholson, S.E., Raghavendra, A., & Jiang, Y. (2016). Possible causes
754 of the Central Equatorial African long-term drought. *Environmental Research Letters, 11*, 124002

755 Huang, D., Knyazikhin, Y., Dickinson, R.E., Rautiainen, M., Stenberg, P., Disney, M., Lewis, P.,
756 Cescatti, A., Tian, Y., Verhoef, W., Martonchik, J.V., & Myneni, R.B. (2007). Canopy spectral
757 invariants for remote sensing and model applications. *Remote Sensing of Environment, 106*, 106-

758   122

759   Huete, A., Didan, K., Miura, T., Rodriguez, E.P., Gao, X., & Ferreira, L.G. (2002). Overview of
760   the radiometric and biophysical performance of the MODIS vegetation indices. *Remote Sensing of*
761   *Environment, 83*, 195-213

762   Huete, A.R., Didan, K., Shimabukuro, Y.E., Ratana, P., Saleska, S.R., Hutyra, L.R., Yang, W.,
763   Nemani, R.R., & Myneni, R. (2006). Amazon rainforests green-up with sunlight in dry season.
764   *Geophysical Research Letters, 33*

765   Huffman, G.J., Bolvin, D.T., Nelkin, E.J., Wolff, D.B., Adler, R.F., Gu, G., Hong, Y., Bowman,
766   K.P., & Stocker, E.F. (2007). The TRMM Multisatellite Precipitation Analysis (TMPA): Quasi-
767   Global, Multiyear, Combined-Sensor Precipitation Estimates at Fine Scales. *Journal of*
768   *Hydrometeorology, 8*, 38-55

769   Jacquemoud, S., Verhoef, W., Baret, F., Bacour, C., Zarco-Tejada, P.J., Asner, G.P., François, C.,
770   & Ustin, S.L. (2009). PROSPECT+SAIL models: A review of use for vegetation characterization.
771   *Remote Sensing of Environment, 113*, S56-S66

772   Jiang, Y., Zhou, L., Tucker, C.J., Raghavendra, A., Hua, W., Liu, Y.Y., & Joiner, J. (2019).
773   Widespread increase of boreal summer dry season length over the Congo rainforest. *Nature*
774   *Climate Change, 9*, 617-+

775   Knyazikhin, Y., Schull, M., Xu, L., Myneni, R., & Samanta, A. (2011). Canopy spectral invariants.
776   Part 1: A new concept in remote sensing of vegetation. *Journal of Quantitative Spectroscopy &*
777   *Radiative Transfer, 112*, 727-735

778   Knyazikhin, Y., Schull, M.A., Stenberg, P., Mottus, M., Rautiainen, M., Yang, Y., Marshak, A.,
779   Latorre Carmona, P., Kaufmann, R.K., Lewis, P., Disney, M.I., Vanderbilt, V., Davis, A.B., Baret,
780   F., Jacquemoud, S., Lyapustin, A., & Myneni, R.B. (2013). Hyperspectral remote sensing of foliar
781   nitrogen content. *Proceedings of the National Academy of Sciences of the United States of America,*
782   *110*, E185-E192

783   Köhler, P., Guanter, L., Kobayashi, H., Walther, S., & Yang, W. (2018). Assessing the potential of
784   sun-induced fluorescence and the canopy scattering coefficient to track large-scale vegetation
785   dynamics in Amazon forests. *Remote Sensing of Environment, 204*, 769-785

786   Lewis, P., & Disney, M.I. (2007). Spectral invariants and scattering across multiple scales from
787   within-leaf to canopy. *Remote Sensing of Environment, 109*, 196-206

788   Li, W., Du, J., Li, S., Zhou, X., Duan, Z., Li, R., Wu, S., Wang, S., & Li, M. (2019). The variation
789   of vegetation productivity and its relationship to temperature and precipitation based on the
790   GLASS-LAI of different African ecosystems from 1982 to 2013. *International Journal of*
791   *Biometeorology, 63*, 847-860

792   Liu, H.Q., & Huete, A. (1995). A Feedback Based Modification of the NDVI to Minimize Canopy
793   Background and Atmospheric Noise. *Ieee Transactions on Geoscience and Remote Sensing, 33*,
794   457-465

Lyapustin, A., Wang, Y., Xiong, X., Meister, G., Platnick, S., Levy, R., Franz, B., Korkin, S., Hilker, T., Tucker, J., Hall, F., Sellers, P., Wu, A., & Angal, A. (2014). Scientific impact of MODIS C5 calibration degradation and C6+ improvements. *Atmospheric Measurement Techniques, 7*, 4353-4365

Marshak, A., & Knyazikhin, Y. (2017). The spectral invariant approximation within canopy radiative transfer to support the use of the EPIC/DSCOVR oxygen B-band for monitoring vegetation. *Journal of Quantitative Spectroscopy and Radiative Transfer, 191*, 7-12

Martínez-Vilalta, J., & Lloret, F. (2016). Drought-induced vegetation shifts in terrestrial ecosystems: The key role of regeneration dynamics. *Global and Planetary Change, 144*, 94-108

Mercado, L.M., Bellouin, N., Sitch, S., Boucher, O., Huntingford, C., Wild, M., & Cox, P.M. (2009). Impact of changes in diffuse radiation on the global land carbon sink. *Nature, 458*, 1014-1017

Moparthy, S., Carrer, D., & Ceamanos, X. (2019). Can We Detect the Brownness or Greenness of the Congo Rainforest Using Satellite-Derived Surface Albedo? A Study on the Role of Aerosol Uncertainties. *Sustainability, 11*, 1410

Morton, D.C., Nagol, J., Carabajal, C.C., Rosette, J., Palace, M., Cook, B.D., Vermote, E.F., Harding, D.J., & North, P.R.J. (2014). Amazon forests maintain consistent canopy structure and greenness during the dry season. *Nature, 506*, 221-224

Mu, Q., Heinsch, F.A., Zhao, M., & Running, S.W. (2007). Development of a global evapotranspiration algorithm based on MODIS and global meteorology data. *Remote Sensing of Environment, 111*, 519-536

Mu, Q., Zhao, M., & Running, S.W. (2011). Improvements to a MODIS global terrestrial evapotranspiration algorithm. *Remote Sensing of Environment, 115*, 1781-1800

Myneni, R.B., Yang, W., Nemani, R.R., Huete, A.R., Dickinson, R.E., Knyazikhin, Y., Didan, K., Fu, R., Negrón Juárez, R.I., Saatchi, S.S., Hashimoto, H., Ichii, K., Shabanov, N.V., Tan, B., Ratana, P., Privette, J.L., Morisette, J.T., Vermote, E.F., Roy, D.P., Wolfe, R.E., Friedl, M.A., Running, S.W., Votava, P., El-Saleous, N., Devadiga, S., Su, Y., & Salomonson, V.V. (2007). Large seasonal swings in leaf area of Amazon rainforests. *Proceedings of the National Academy of Sciences, 104*, 4820-4823

Ndehedehe, C.E., Ferreira, V.G., & Agutu, N.O. (2019). Hydrological controls on surface vegetation dynamics over West and Central Africa. *Ecological Indicators, 103*, 494-508

Nicholson, S.E. (2018). The ITCZ and the Seasonal Cycle over Equatorial Africa. *Bulletin of the American Meteorological Society, 99*, 337-348

Oliveira, R.S., Dawson, T.E., Burgess, S.S.O., & Nepstad, D.C. (2005). Hydraulic redistribution in three Amazonian trees. *Oecologia, 145*, 354-363

Philippon, N., Cornu, G., Monteil, L., Gond, V., Moron, V., Pergaud, J., Sèze, G., Bigot, S.,

831 Camberlin, P., Doumenge, C., Fayolle, A., & Ngomanda, A. (2019). The light-deficient climates
832 of western Central African evergreen forests. *Environmental Research Letters, 14*, 034007

833 Piao, S., Wang, X., Park, T., Chen, C., Lian, X., He, Y., Bjerke, J.W., Chen, A., Ciais, P.,
834 Tømmervik, H., Nemani, R.R., & Myneni, R.B. (2020). Characteristics, drivers and feedbacks of
835 global greening. *Nature Reviews Earth & Environment, 1*, 14-27

836 Pierret, A., Maeght, J.-L., Clément, C., Montoroi, J.-P., Hartmann, C., & Gonkhamdee, S. (2016).
837 Understanding deep roots and their functions in ecosystems: an advocacy for more unconventional
838 research. *Annals of Botany, 118*, 621-635

839 Pires, G.F., & Costa, M.H. (2013). Deforestation causes different subregional effects on the
840 Amazon bioclimatic equilibrium. *Geophysical Research Letters, 40*, 3618-3623

841 Raghavendra, A., Zhou, L., Jiang, Y., & Hua, W. (2018). Increasing extent and intensity of
842 thunderstorms observed over the Congo Basin from 1982 to 2016. *Atmospheric Research, 213*,
843 17-26

844 Raghavendra, A., Zhou, L., Roundy, P.E., Jiang, Y., Milrad, S.M., Hua, W., & Xia, G. (2020). The
845 MJO's impact on rainfall trends over the Congo rainforest. *Climate Dynamics, 54*, 2683-2695

846 Rouse, J.W., Haas, R.H., Schell, J.A., & Deering, D.W. (1974). Monitoring Vegetation Systems in
847 the Great Plains with Erts. In, *Third Earth Resources Technology Satellite-1 Symposium- Volume
848 I: Technical Presentations*. Washington, D.C.: NASA

849 Rutan, D.A., Kato, S., Doelling, D.R., Rose, F.G., Nguyen, L.T., Caldwell, T.E., & Loeb, N.G.
850 (2015). CERES Synoptic Product: Methodology and Validation of Surface Radiant Flux. *Journal
851 of Atmospheric and Oceanic Technology, 32*, 1121-1143

852 Samanta, A., Knyazikhin, Y., Xu, L., Dickinson, R.E., Fu, R., Costa, M.H., Saatchi, S.S., Nemani,
853 R.R., & Myneni, R.B. (2012). Seasonal changes in leaf area of Amazon forests from leaf flushing
854 and abscission. *Journal of Geophysical Research: Biogeosciences, 117*

855 Song, W., Knyazikhin, Y., Wen, G., Marshak, A., Mõttus, M., Yan, K., Yang, B., Xu, B., Park, T.,
856 & Chen, C. (2018). Implications of Whole-Disc DSCOVR EPIC Spectral Observations for
857 Estimating Earth's Spectral Reflectivity Based on Low-Earth-Orbiting and Geostationary
858 Observations. *Remote Sensing, 10*, 1594

859 Sorí, R., Nieto, R., Vicente-Serrano, S.M., Drumond, A., & Gimeno, L. (2017). A Lagrangian
860 perspective of the hydrological cycle in the Congo River basin. *Earth System Dynamic, 8*, 653-
861 675

862 Wan, Z. (2014). New refinements and validation of the collection-6 MODIS land-surface
863 temperature/emissivity product. *Remote Sensing of Environment, 140*, 36-45

864 Wang, D., Morton, D., Masek, J., Wu, A., Nagol, J., Xiong, X., Levy, R., Vermote, E., & Wolfe, R.
865 (2012). Impact of sensor degradation on the MODIS NDVI time series. *Remote Sensing of
866 Environment, 119*, 55-61

867 Wang, Y., Buermann, W., Stenberg, P., Smolander, H., H‰me, T., Tian, Y., Hu, J., Knyazikhin, Y.,
868 & Myneni, R.B. (2003). A new parameterization of canopy spectral response to incident solar
869 radiation: case study with hyperspectral data from pine dominant forest. *Remote Sensing of*
870 *Environment, 85*, 304-315

871 Xu, L., Saatchi, S.S., Yang, Y., Myneni, R.B., Frankenberg, C., Chowdhury, D., & Bi, J. (2015).
872 Satellite observation of tropical forest seasonality: spatial patterns of carbon exchange in
873 Amazonia. *Environmental Research Letters, 10*, 084005

874 Xu, L., Samanta, A., Costa, M.H., Ganguly, S., Nemani, R.R., & Myneni, R.B. (2011). Widespread
875 decline in greenness of Amazonian vegetation due to the 2010 drought. *Geophysical Research*
876 *Letters, 38*

877 Yan, D., Zhang, X., Yu, Y., & Guo, W. (2016a). A Comparison of Tropical Rainforest Phenology
878 Retrieved From Geostationary (SEVIRI) and Polar-Orbiting (MODIS) Sensors Across the Congo
879 Basin. *IEEE Transactions on Geoscience and Remote Sensing, 54*, 4867-4881

880 Yan, D., Zhang, X., Yu, Y., & Guo, W. (2017). Characterizing Land Cover Impacts on the
881 Responses of Land Surface Phenology to the Rainy Season in the Congo Basin. *Remote Sensing,*
882 *9*, 461

883 Yan, K., Park, T., Yan, G., Chen, C., Yang, B., Liu, Z., Nemani, R.R., Knyazikhin, Y., & Myneni,
884 R.B. (2016b). Evaluation of MODIS LAI/FPAR Product Collection 6. Part 1: Consistency and
885 Improvements. *Remote Sensing, 8*, 359

886 Yan, K., Park, T., Yan, G., Liu, Z., Yang, B., Chen, C., Nemani, R.R., Knyazikhin, Y., & Myneni,
887 R.B. (2016c). Evaluation of MODIS LAI/FPAR Product Collection 6. Part 2: Validation and
888 Intercomparison. *Remote Sensing, 8*, 460

889 Yang, B., Knyazikhin, Y., Mottus, M., Rautiainen, M., Stenberg, P., Yan, L., Chen, C., Yan, K.,
890 Choi, S., Park, T., & Myneni, R.B. (2017). Estimation of leaf area index and its sunlit portion from
891 DSCOVR EPIC data: Theoretical basis. *Remote Sensing of Environment, 198*, 69-84

892 Yang, J., Tian, H., Pan, S., Chen, G., Zhang, B., & Dangal, S. (2018a). Amazon drought and forest
893 response: Largely reduced forest photosynthesis but slightly increased canopy greenness during
894 the extreme drought of 2015/2016. *Global Change Biology, 24*, 1919-1934

895 Yang, Y., Saatchi, S.S., Xu, L., Yu, Y., Choi, S., Phillips, N., Kennedy, R., Keller, M., Knyazikhin,
896 Y., & Myneni, R.B. (2018b). Post-drought decline of the Amazon carbon sink. *Nature*
897 *Communications, 9*, 3172

898 Zhang, Y., Song, C., Band, L.E., Sun, G., & Li, J. (2017). Reanalysis of global terrestrial vegetation
899 trends from MODIS products: Browning or greening? *Remote Sensing of Environment, 191*, 145-
900 155

901 Zhou, L., Tian, Y., Myneni, R.B., Ciais, P., Saatchi, S., Liu, Y.Y., Piao, S., Chen, H., Vermote, E.F.,
902 Song, C., & Hwang, T. (2014). Widespread decline of Congo rainforest greenness in the past
903 decade. *Nature, 509*, 86-90
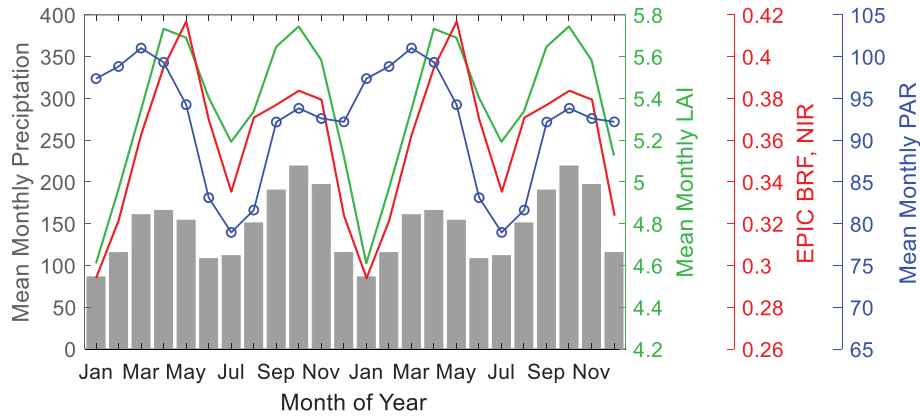
Fig. 1. Annual course of monthly-average precipitation, PAR, LAI, EPIC NIR BRF over the Congolese forests. The annual cycle is repeated two times for better demonstration. Precipitation, LAI and NIR BRF clear show bimodal variations with peaks in March-April-May (MAM, wet season 1) and September-October-November (SON, wet season 2).
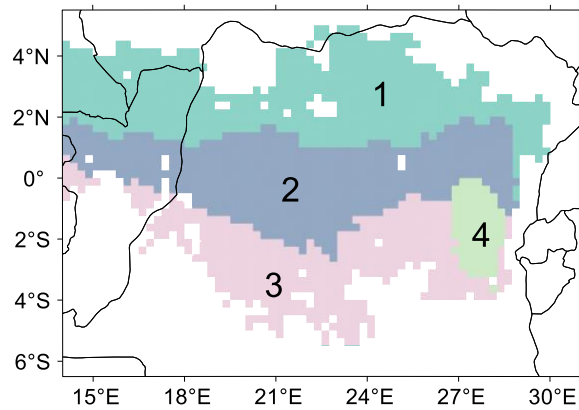

Fig. 2. Four phenological regions clustered based on normalized 20-year mean monthly climatology of precipitation, PAR and LAI data using K-Means clustering method. Region 4 (0.2°S-3°S, 26.8°E-28.5°E) represents montane forests located at moderate elevations between 530 m and 1728 m.
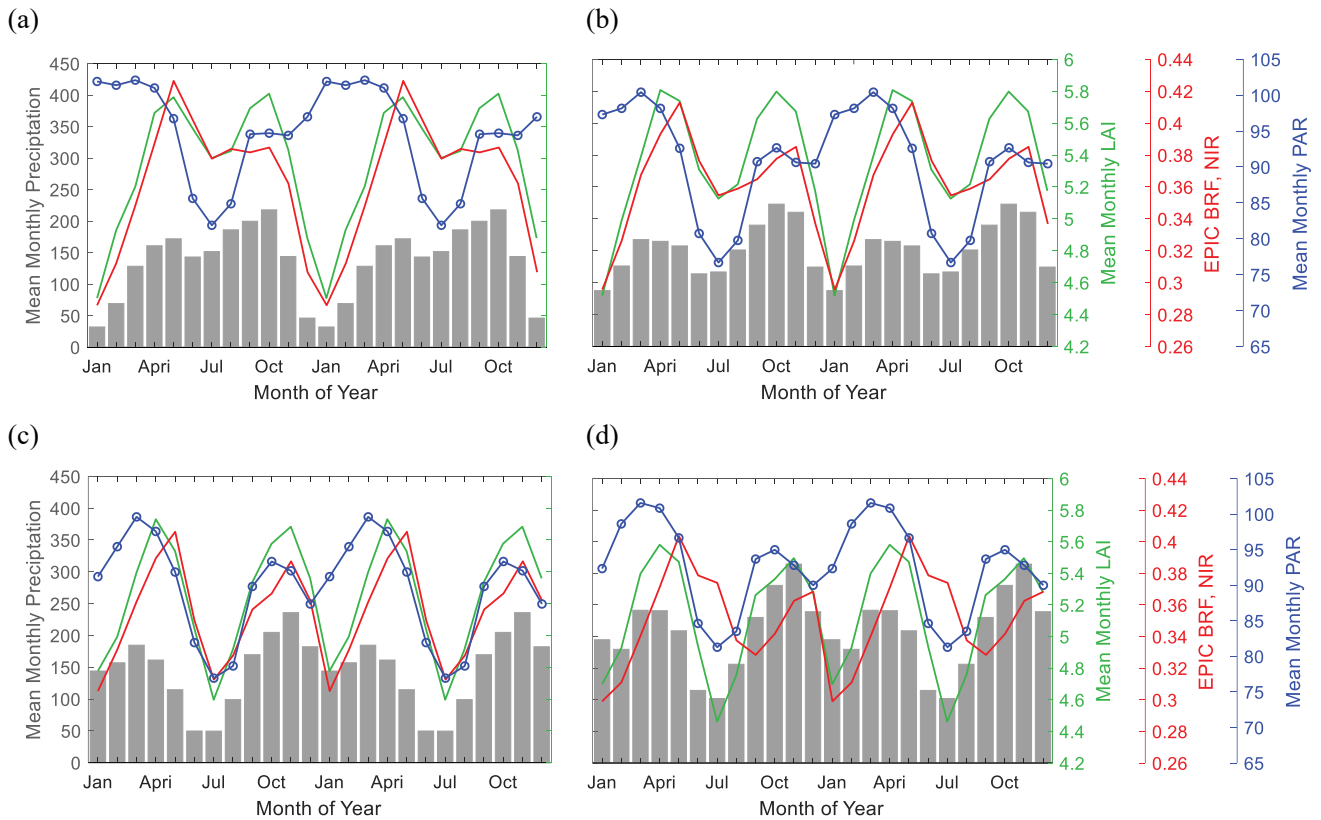
Fig. 3. Annual course of monthly-average precipitation, PAR, LAI, EPIC NIR BRF over (a) region 1, (b) region 2, (c) region 3 and (d) region 4. Phenological regions are shown in Figure 2. The annual cycles are replicated two times for better demonstration. The peak-to-peak amplitude of bimodal curves tends to increase from north (region 1) to south (region 3).
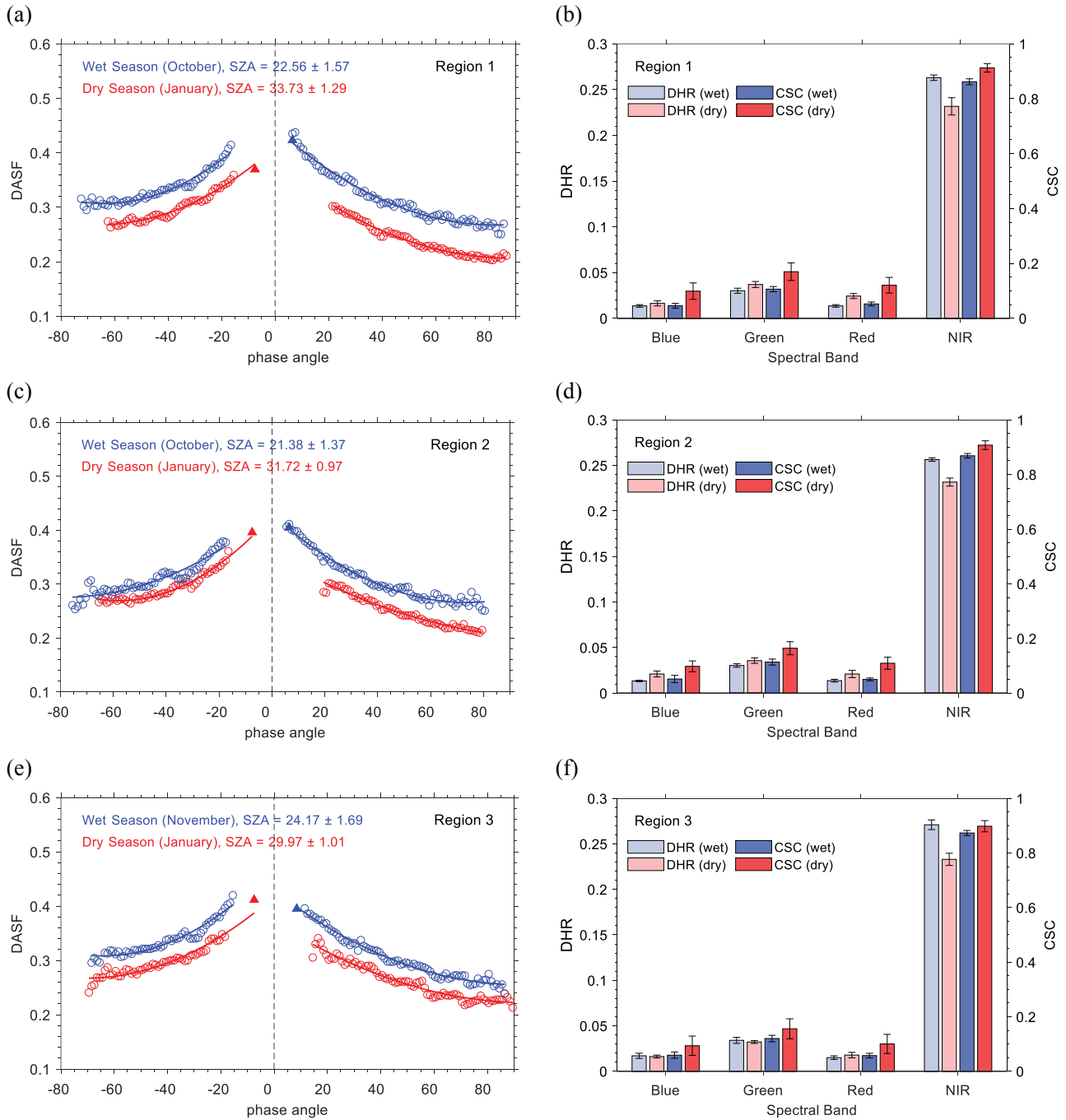
Fig. 4. Directional Area Scattering Factors (DASF) derived from MISR and DSCOVR EPIC data (left panels), MISR Directional Hemispherical Reflectances (DHR) and Canopy Scattering Coefficients (CSC) during wet and dry seasons over region 1 (panels a and b), region 2 (panels c and d) and region 3 (panels e and f). The circles and solid triangles represent MISR and DSCOVR EPIC observations. The lines show polynomial fits to MISR data. There were no enough valid reflectance data over region 3 in October. Therefore, we use November to represent the dry season in this region.
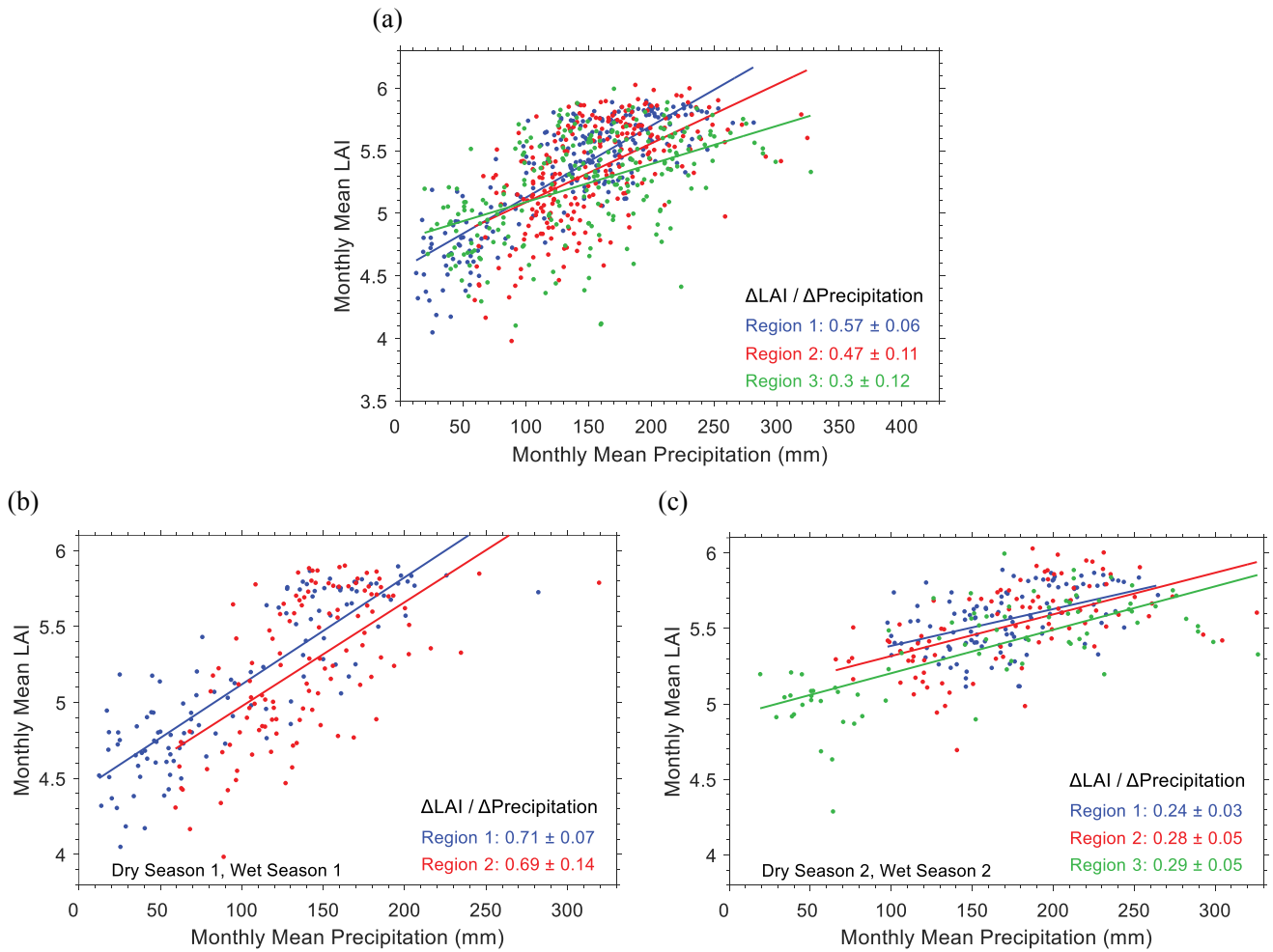
Fig. 5. Relationship between regional monthly precipitation and LAI during (a) full annual seasonal cycle, (b) seasonal cycle 1 (December-May) and (c) cycle 2 (June-November). Slopes of the regression lines are taken as a measure of LAI sensitivity to changes in in the precipitation (ΔLAI/ΔPrecipitation).
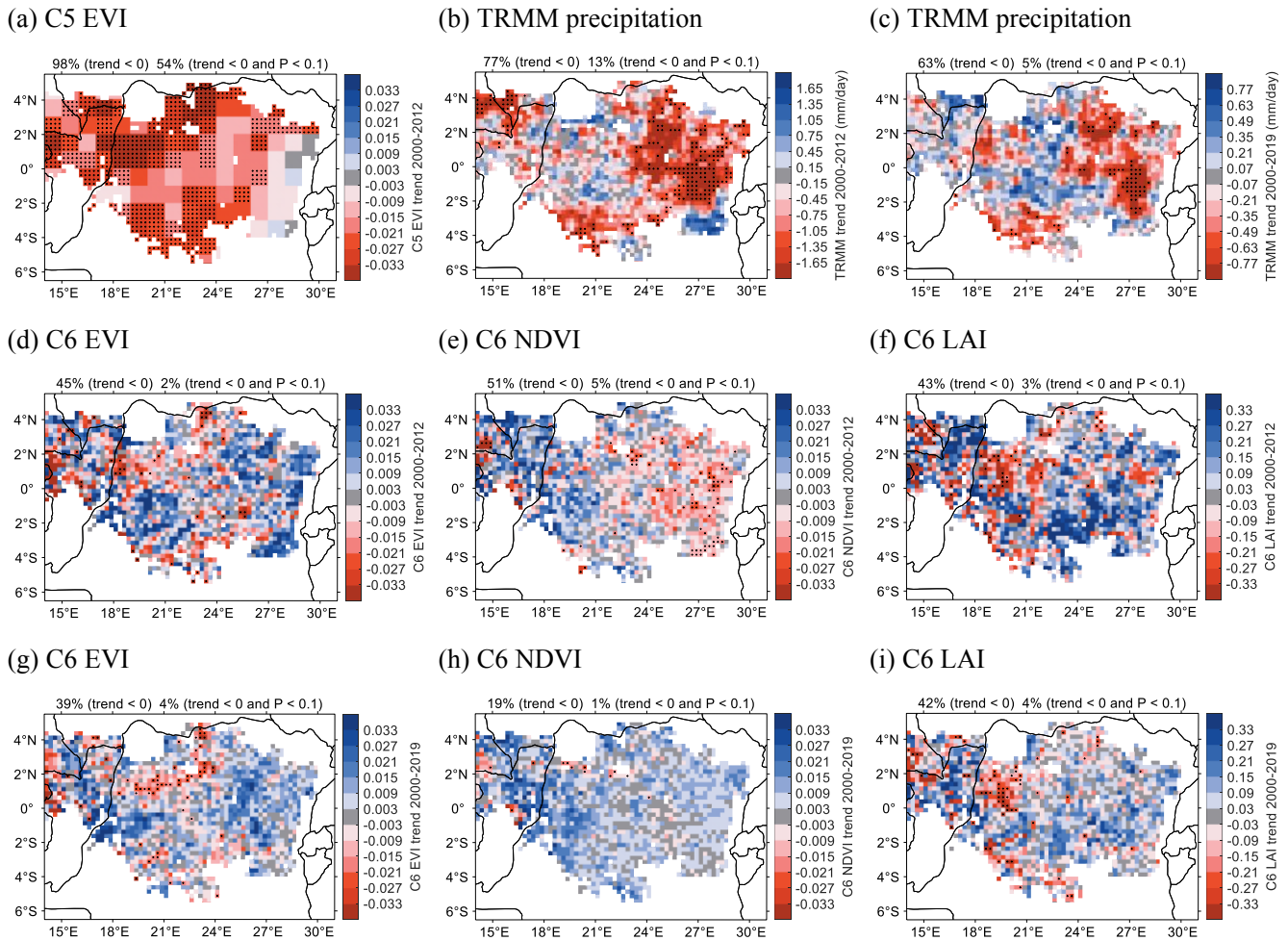
Fig. 6. Linear trends per decade in April-May-June for the period of 2000-2012 and 2000-2019. Pixels with the plus symbol indicate statistically significant trends (P<0.1). Percentages of pixels with negative trends and negative trends at P<0.1 are shown above each plot. The upper plots show trends in MODIS Collection 5 EVI from 2000 to 2012 (panel a) and TRMM precipitations for the 2000 to 2012 (panel b) and 2000 to 2019 (panel c) periods. Trends in MOIDIS Collection 6 EVI, NDVI and LAI for the 2000 to 2012 and the 2000 to 2019 periods are shown in middle and lower plots, respectively.
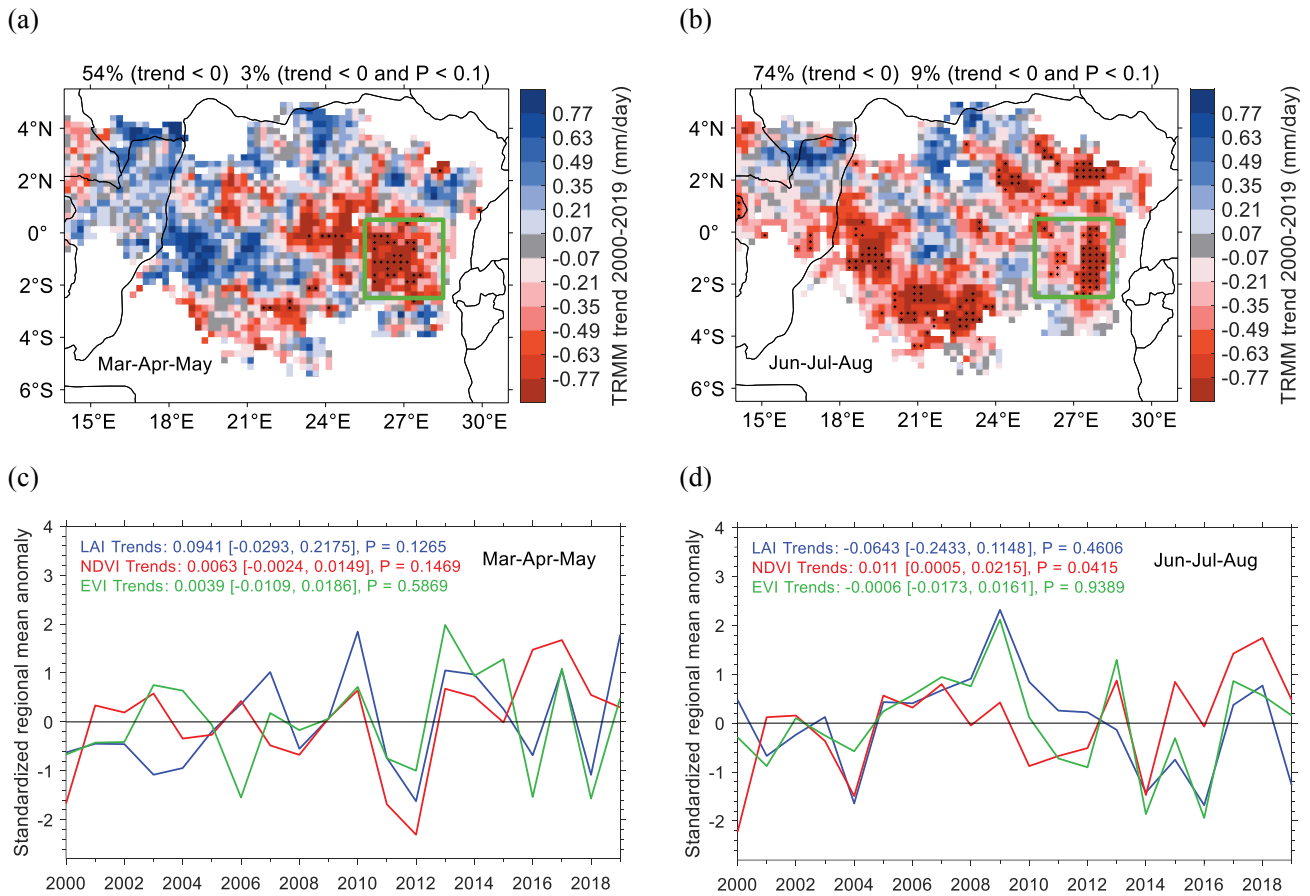
Fig. 7. Upper panels. Precipitation linear trends per decade during (a) wet season 1 (MAM) and (b) dry season 2 (JJA) for the period of 2000-2019. Pixels with the plus symbols indicate statistically significant trends (P<0.1). A region between 0.5°N-2.5°S and 25.5°E-28.5°E where a significant precipitation decline was observed both during the wet and dry seasons is shown as a green rectangle. Lower panels. Standardized regional mean anomalies in LAI, NDVI and EVI for the selected region during (c) wet (MAM) and (d) dry (JJA) seasons for the 2000-2019 period. The linear trend (with 95% confidence interval) per decade and its significance level P are shown in legends.
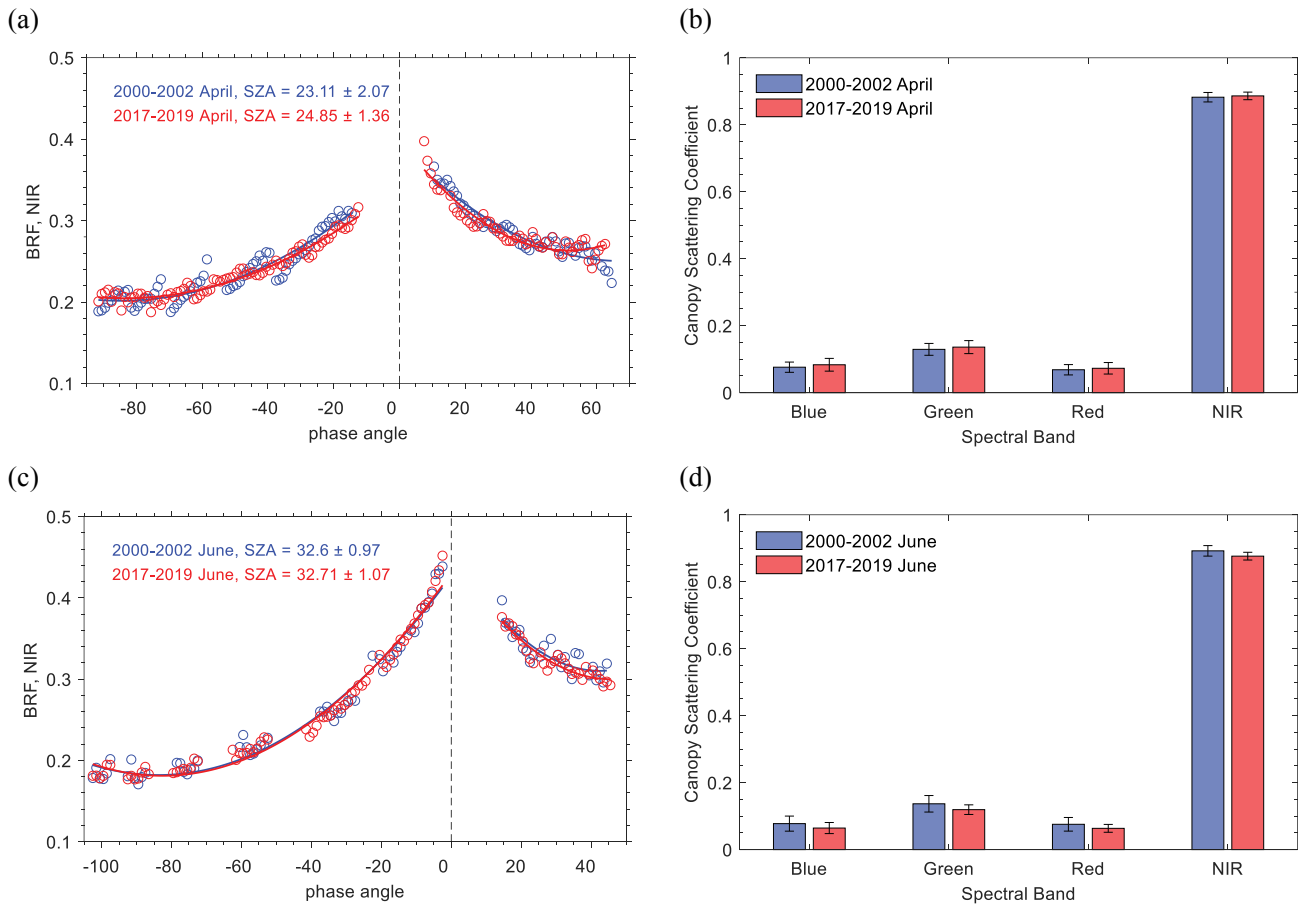
Fig. 8. MISR BRF at NIR (866 nm) and canopy scattering coefficient (right panels) of the region with significant drought at the beginning (2000-2002) and at the end (2017-2019) of the 2000-2019 observation period. Upper and lower panels show BRF and the coefficient in April (wet season) and June (dry season), respectively. These variables other months show similar behavior.

Supplementary Information
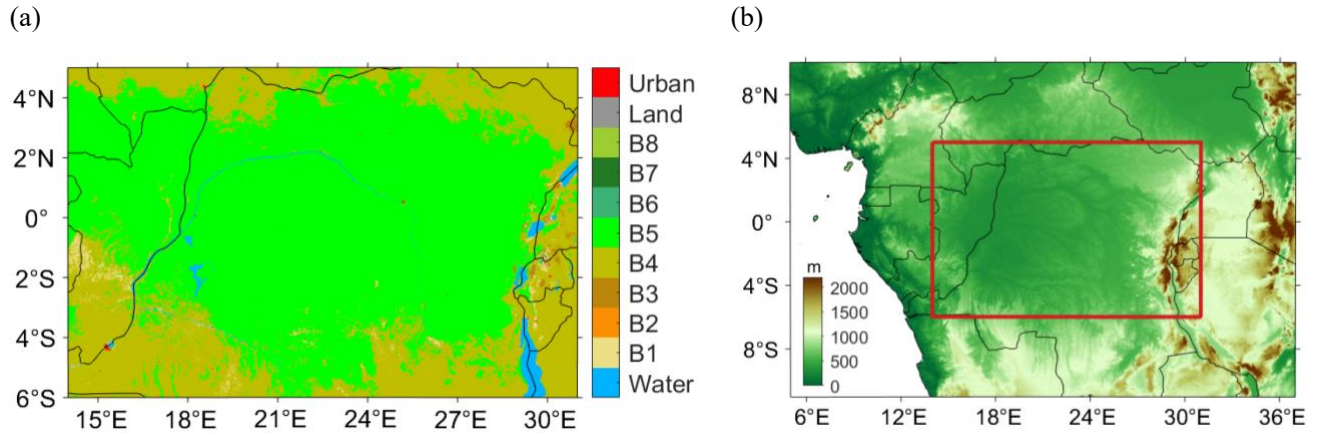
Figure S1. (a) Landcover of the Congo Basin (5°N-6°S, 14°E-31°E) in Year 2010 according to the MODIS LAI classification scheme. It stratifies the global vegetation into eight architectural types, or biomes: grasslands (B1), shrublands (B2), broadleaf croplands (B3), savannas (B4), evergreen broadleaf forest (B5), deciduous broadleaf forests (B6), evergreen needleleaf forests (B7), deciduous needleleaf forests (B8). Biome types present in the Congo Basin are evergreen broadleaf forest (B5) and savannas (B4). (b) Terrain elevation from SRTM dataset. Our study area is shown as a red rectangle. Elevation of a highland region in the southeast part of the study area varies between 530 m and 1728 m. This area represents a montane ecosystem.
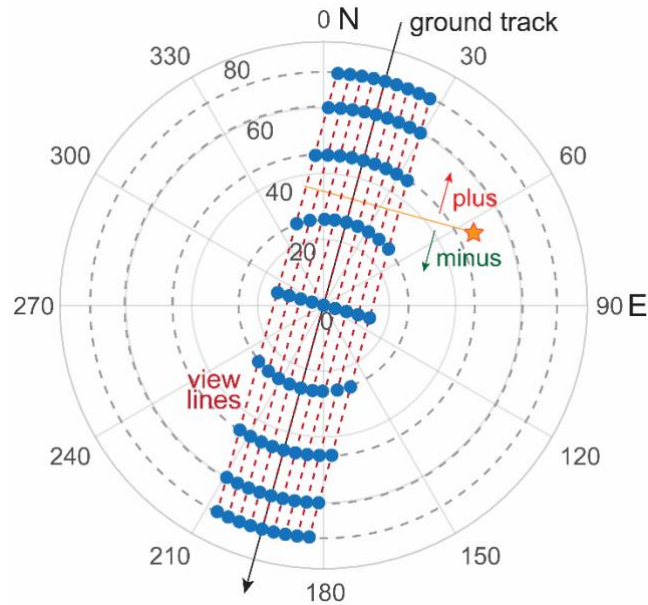
Figure S2. Sun-sensor geometry of MISR observations on the polar plane. Direction from a point on the Earth surface to Sun is shown as a star. The MISR instrument uses nine separate forward-, nadir- and aft-looking push broom cameras to acquire data at nine along-track view zenith angles of 0.0º (camera An), 26.1º (Af and Aa), 45.6º (Bf and Ba), 60.0º (Cf and Ca) and 70.5º (Df and Da). Each camera sees instantaneously a single row of pixels at right angles to the ground track, resulting in a 360 km cross-track swath. MISR along-track observation angles form lines on the polar plane, which are characterized by a slope, k, and intercept, b. The slope is constant ($k \sim \tan(15.4º)$) and coincides with the ground track direction (~15.4º). The intercept is associated with location of pixel within the 360 km swath that cameras see. We express BRF as a function of the phase angle, which is the angle between directions to the sun and sensor. We assign the sign "plus" to the phase angle if the direction to the MISR sensor approaches the direction to sun from North, and "minus" otherwise. In this sun-tracking coordinates the MISR Bidirectional Reflectance Factor (BRF) is a function of SZA, phase angle and MISR view line, the latter is specified by VZA of the MISR nadir camera.
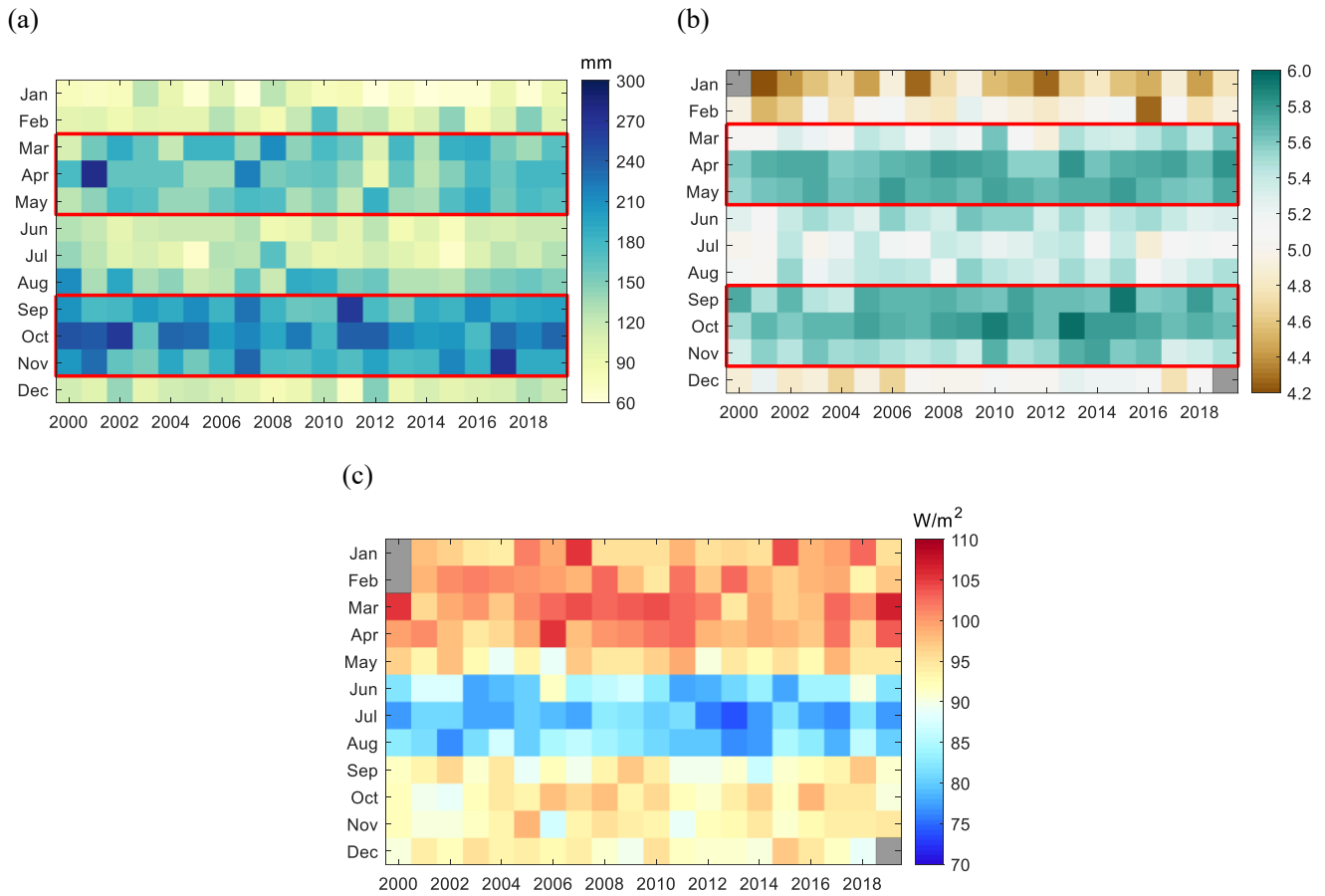
Figure S3. Seasonality of (a) monthly precipitation from TRMM, (b) LAI from MODIS C6 and (c) PAR from CERES over the Congolese forests in the past two decades (2000-2019). Months with no data are labeled with grey color in the color maps. A bimodal seasonal cycle is clearly seen in the rainfall and the LAI color maps. The first peak in precipitation and LAI occurred in March-April-May (wet season 1) and the second in September-October-November (wet season 2). Wet season periods are marked with red square in the (a) and (b).
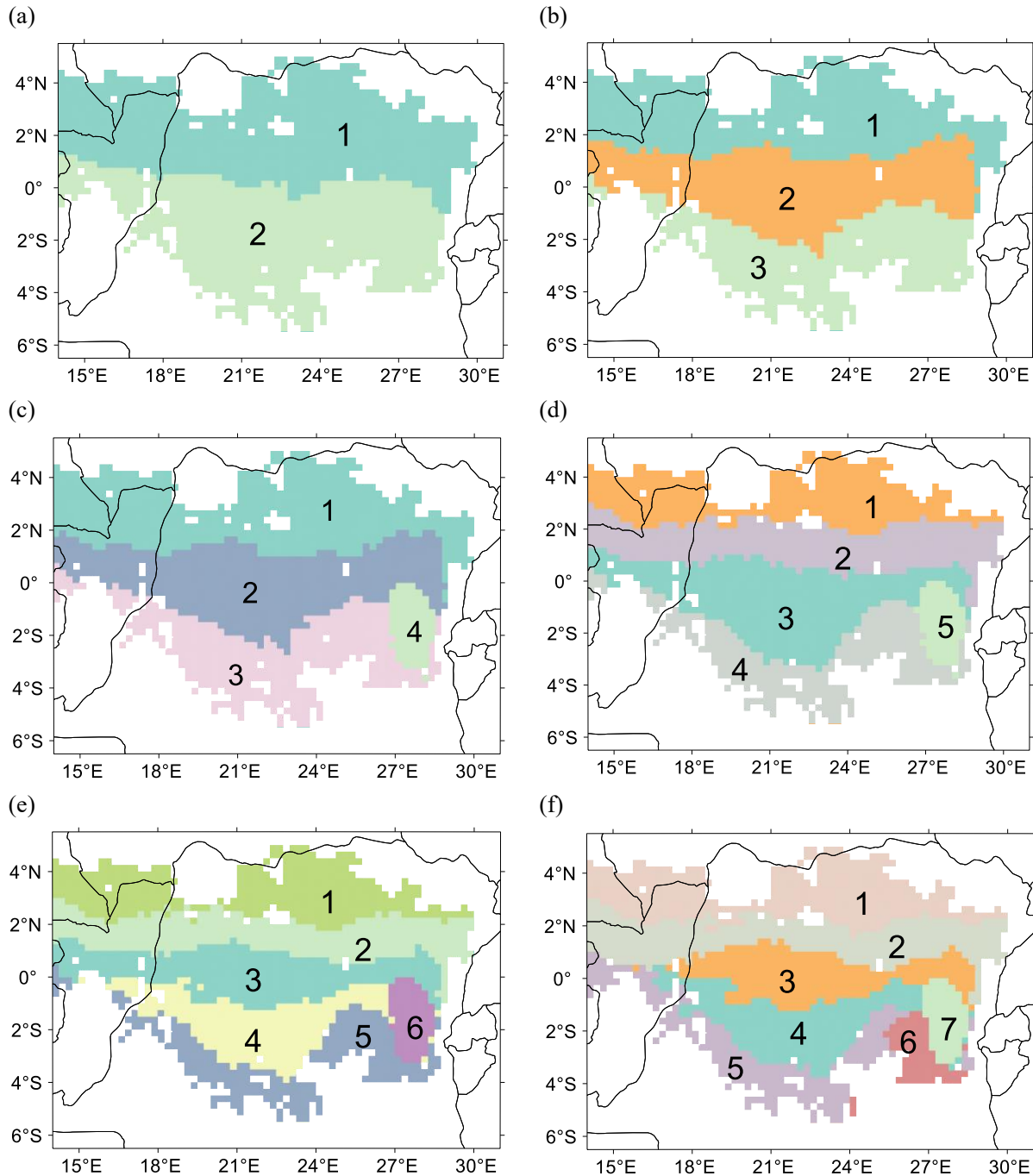
Figure S4. Partitioning of the study area into 2 to 7 clusters. K-Means clustering method with mean monthly climatology data of precipitation, PAR and LAI as input was used. Boundaries of clusters are generally parallel to the Equator. A highland region in the southeast part the Congolese forest (Figure S1) appeared in partitioning our study area into 4 and more clusters. An increase in the number of clusters lowers cluster areas, which in turn may not contain enough satellite observations for statistical analyses. We use the four-cluster partition in our analyses.
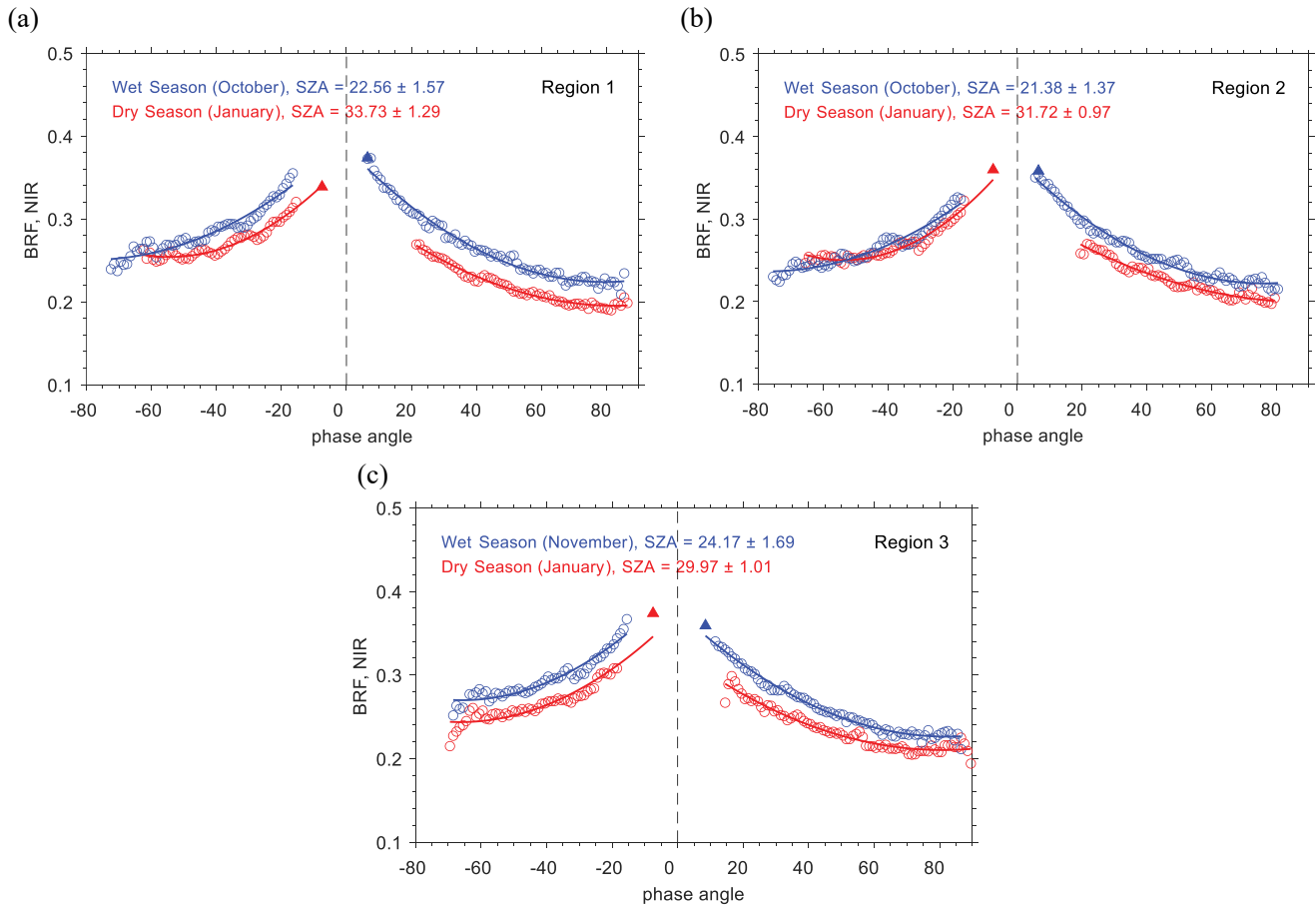
Figure S5. MISR BRF and DSCOVR BRF at NIR spectral bands during the wet and dry seasons over region 1 (panel a), region 2 (panel c) and region 3 (panel c). Note that a higher or equal reflectance at lower SZA relative to reflectance at higher SZA always indicates an increase in leaf area and foliage scattering properties according to the physics of radiation interaction in vegetation (Bi et al., 2015). Such a behavior is clearly seen in BRF of region 2.
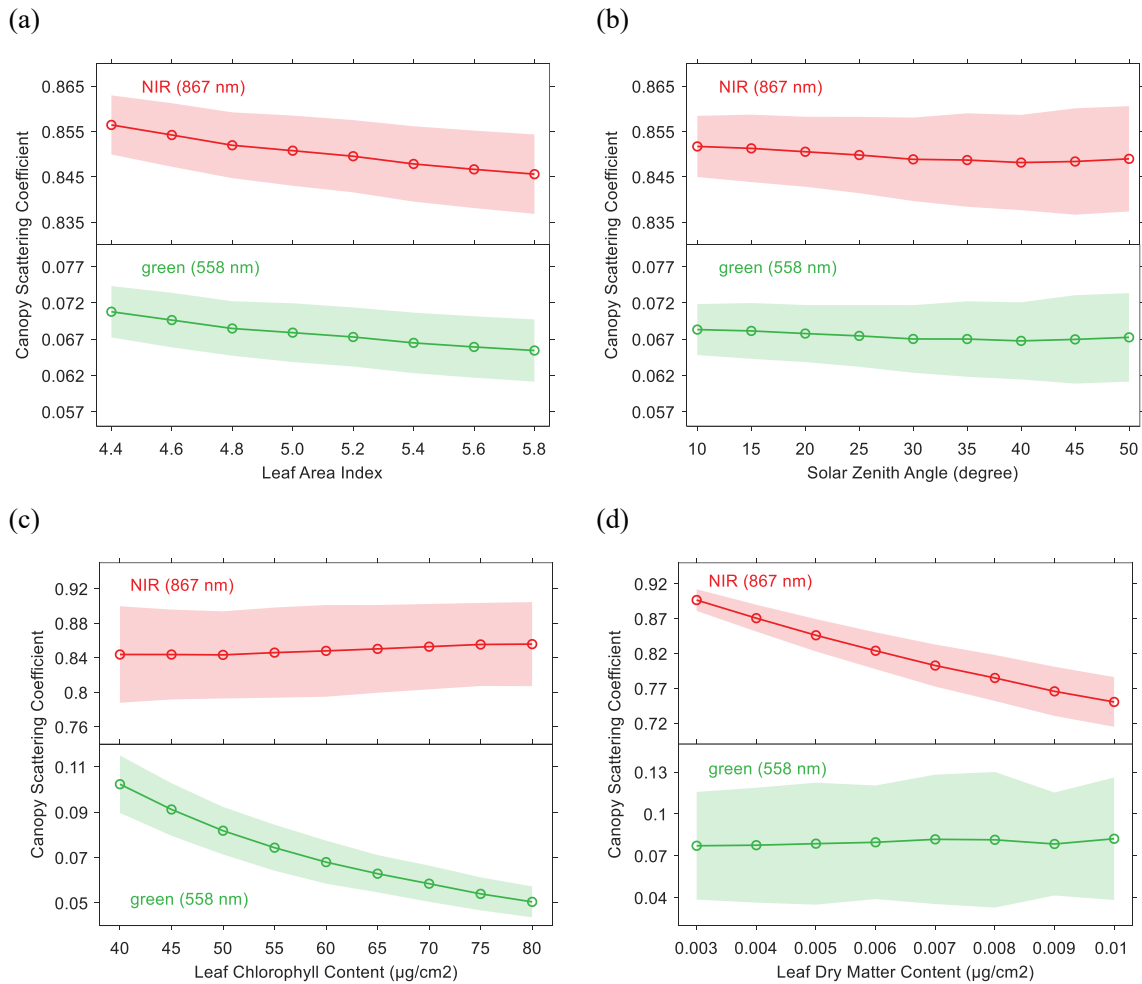
Figure S6. Sensitivity of the canopy scattering coefficient to (a) LAI, LAI>4.4, (b) SZA, (c) leaf chlorophyll content and (d) leaf dry matter content in green (558nm) and NIR (867 nm) derived based on the PROSAIL model (Jacquemoud et al. 2009). The shaded area represents the ±1 standard deviation error. The canopy scattering coefficient is almost insensitive to LAI and SZA, but exhibits strong sensitive to leaf chlorophyll and dry matter contents in green (558 nm) and NIR (867 nm), respectively.
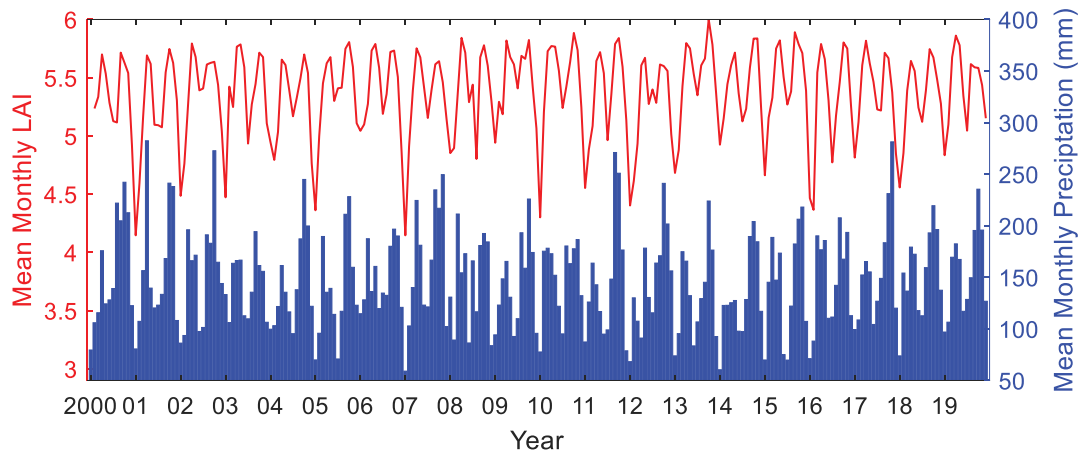
Figure S7. Time series of monthly LAI and precipitation from 2000 to 2019 over the Congolese forests. The MODIS Collection 6 LAI product and TRMM 3B43 version 7 data were used to generate monthly average LAI and precipitation time series as described in Section 2. The monthly LAI and precipitation are strongly positively correlated (R=0.67, P<0.01), suggesting a direct and instant impact of water availability on the functionality the Congolese forests.
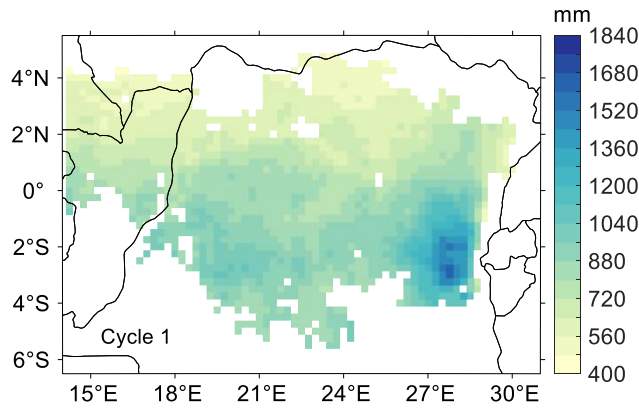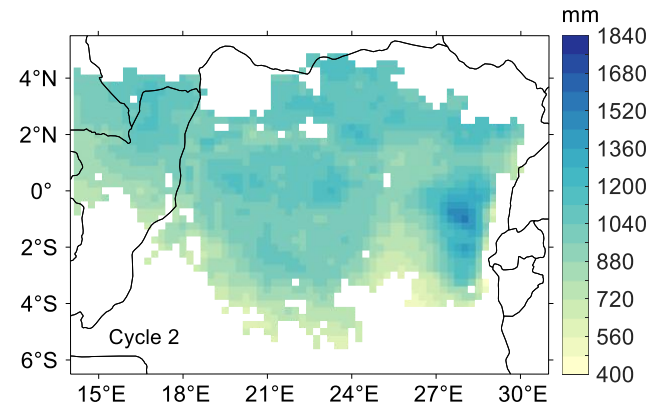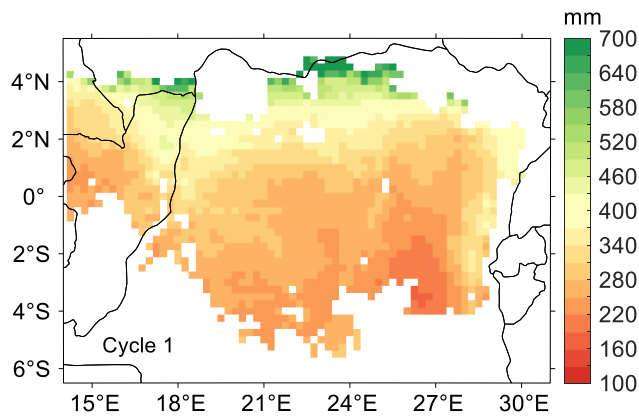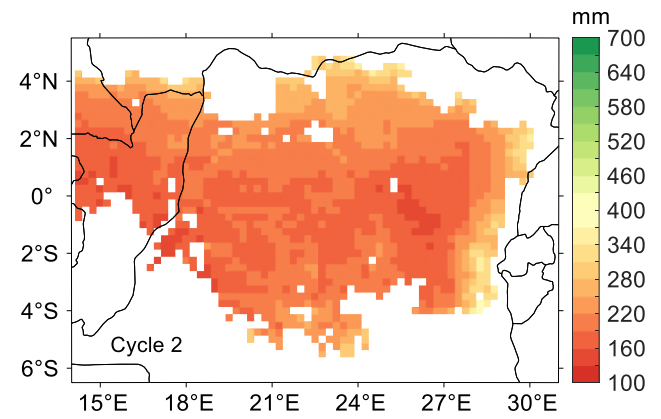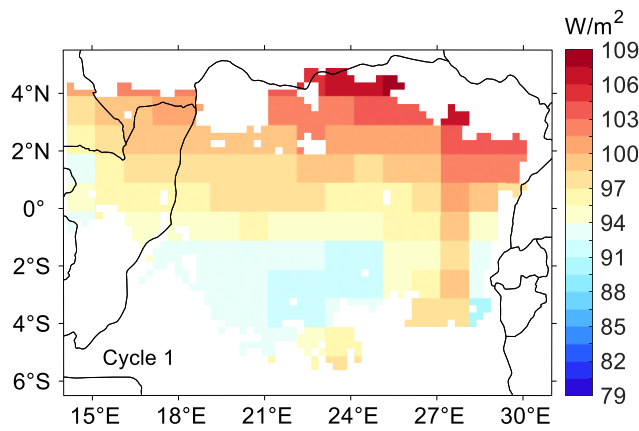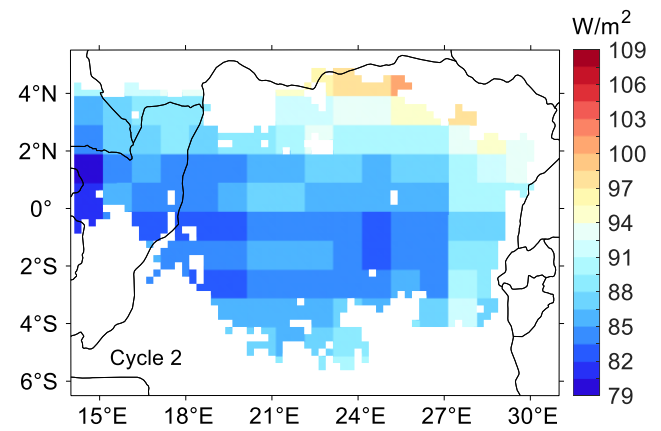
Figure S8. Distribution of precipitation, climatic water deficit and PAR during seasonal cycles 1 (December to June, left panels) and 2 (June to December, right panels).
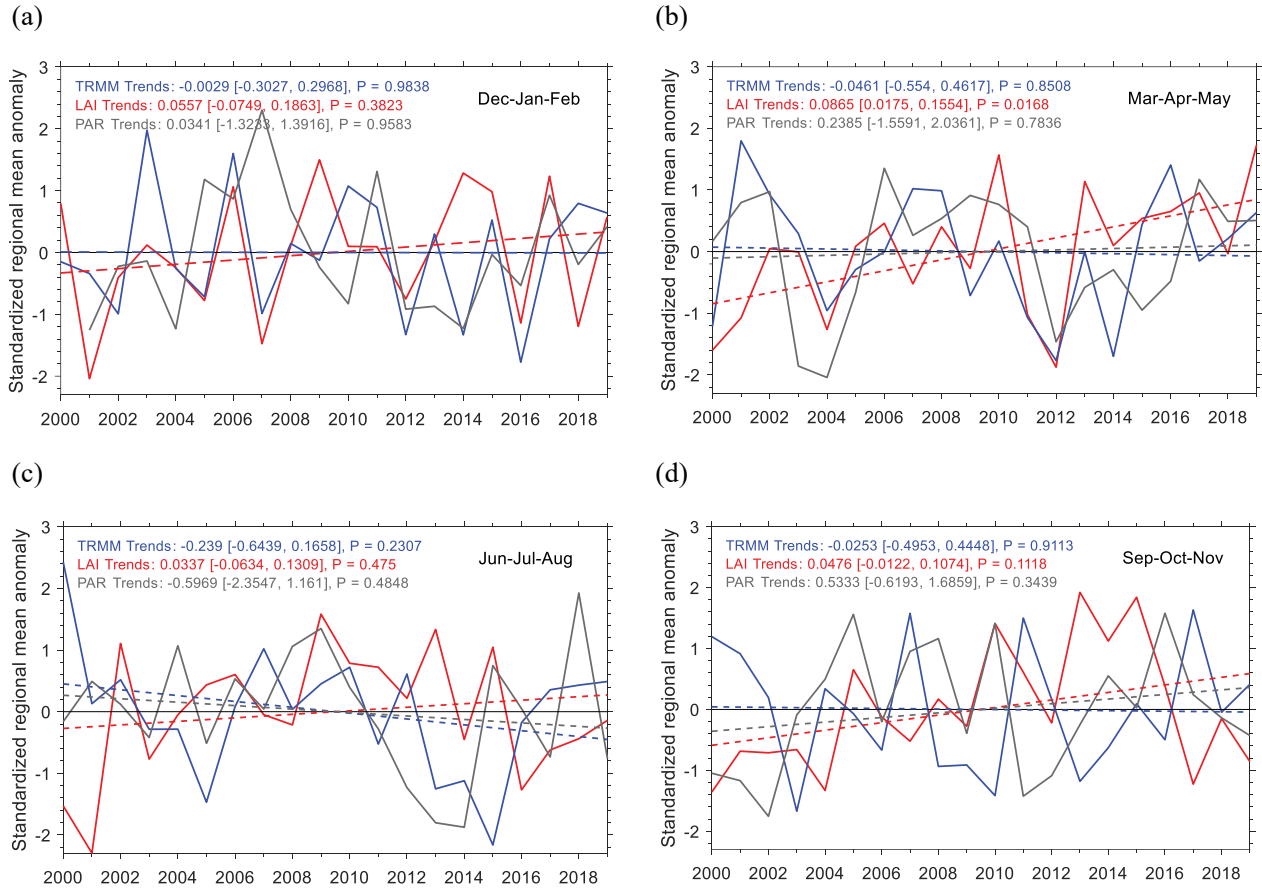
Figure S9. Standardized regional mean anomalies in seasonal precipitation, LAI and PAR for seasonal cycles 1 (upper panels) and 2 (lower panels) over the entire Congolese forests for the period of 2000-2019. Values of linear trends (with 95% confidence interval) per decade and their significant levels, P, are shown in legends. There are no significant declines or increases in precipitation and PAR for the past two decades. All seasons have shown an increase in LAI with a higher P-values during wet seasons.
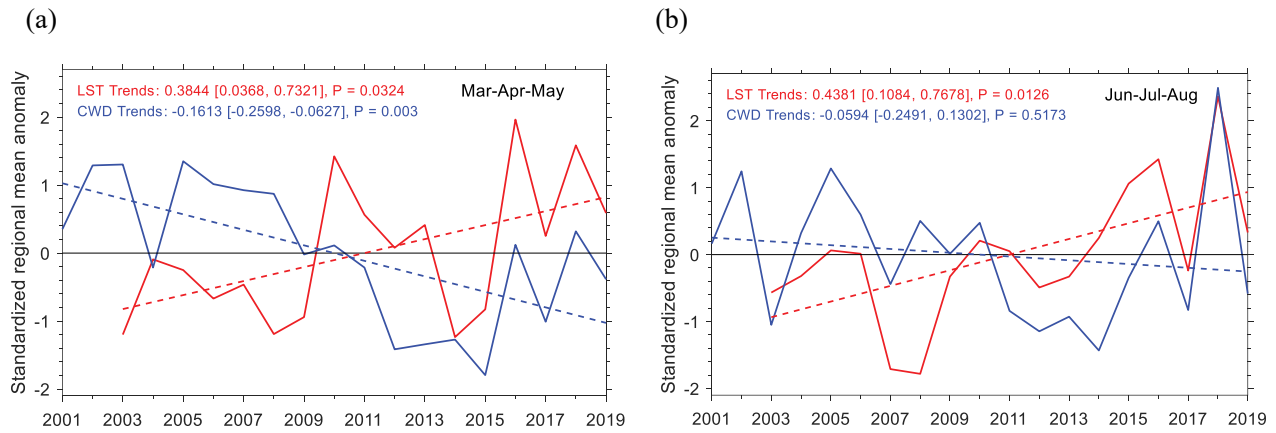
(a)

(b)

Figure S10. Standardized regional mean anomalies in seasonal land surface temperature (LST) and climatic water deficit (CWD) over the focus region (0.5°N-2.5°S, 25.5°E-28.5°E) for the past two decades in wet season 1 (MAM) and dry season 2 (JJA). The linear trend (with 95% confidence interval) per decade and its significant level P are shown.